Geophysical Research Letters

RESEARCH LETTER
10.1029/2025GL121051

Atmospheric Dynamics of IR-Active Particles Released From Mars' Surface

Mark I. Richardson[1], Samaneh Ansari[2], Bowen Fan[3,4], Ramses Ramirez[5], Hooman Mohseni[2], Michael A. Mischna[6], Michael H. Hecht[7], Liam J. Steele[3,8], Felix Sharipov[9], and Edwin S. Kite[3]

[1]Aeolis Research, Chandler, AZ, USA, [2]Northwestern University, Evanston, IL, USA, [3]University of Chicago, Chicago, IL, USA, [4]Now at Yale University, New Haven, CT, USA, [5]University of Central Florida, Orlando, FL, USA, [6]Jet Propulsion Laboratory, California Institute of Technology, Pasadena, CA, USA, [7]MIT Haystack Observatory, Westford, MA, USA, [8]Now at European Center for Medium-Range Weather Forecasts, Reading, UK, [9]Universidade Federal do Paraná, Curitiba, Brazil

Key Points:

- Using a plume-tracking climate model, we investigate radiative-dynamical feedback from release of two particle compositions at Mars' surface
- For a single, constant source, global particle abundance saturates in no more than 4 Mars Years, enabling Mars surface and atmospheric warming
- Self-lofting helps particles rise and spread, and an enhanced Hadley cell aids global mixing

Supporting Information:

Supporting Information may be found in the online version of this article.

Correspondence to:

M. I. Richardson and E. S. Kite,
mir@aeolisresearch.com;
kite@uchicago.edu

Citation:

Richardson, M. I., Ansari, S., Fan, B., Ramirez, R., Mohseni, H., Mischna, M. A., et al. (2026). Atmospheric dynamics of IR-active particles released from Mars' surface. *Geophysical Research Letters*, *53*, e2025GL121051. https://doi.org/10.1029/2025GL121051

Received 9 DEC 2025
Accepted 3 MAR 2026

Abstract Surface release of radiatively active particles, with high infrared- (IR-)to-visible extinction ratios, has been proposed as a method of warming Mars. However, to warm Mars using aerosols, particles released locally must disperse globally. Here we provide an initial reference study in a plume tracking, dry Martian atmospheric model to address this question. The winds that transport aerosols respond to the aerosol's IR forcing, implying strong radiative-dynamical feedbacks (RDF). We investigate RDF from surface release of two particle compositions: carbon (graphene) and metal (Al). Self-lofting helps particles rise and spread locally and regionally, and the Hadley cell strengthens under warming, aiding latitudinal mixing. Within our model, Mars RDF enable engineered-aerosol warming. Warming is slightly greater for three-dimensional vs. 1D-models and also depends on spectral resolution of radiative transfer. We assess implications for Mars warming. Many open atmospheric science questions remain, including the role of agglomeration, dry-deposition rate uncertainty, and modeling water cycle feedbacks.

Plain Language Summary Both aerosols and gases have been proposed as ways of warming Mars. For the aerosol method, particles released locally must disperse globally. We address this question for the first time using a plume-tracking, dry Martian global atmospheric model. We find that for a single, constant source, global particle abundance saturates in <4 Mars Years, enabling Mars surface and atmospheric warming. Self-lofting helps particles rise and spread, and stronger winds help global mixing. Warming is strong, but varies depending on model set-up (stronger in 3-D models than in 1-D models). Many open atmospheric science questions remain, including the role of agglomeration, dry-deposition rate uncertainty, and modeling water cycle feedbacks.

1. Introduction

Mars is a cold desert, with a weak greenhouse effect (+5 K from its 6 mbar CO_2 atmosphere), abundant frozen H_2O (Carr & Head, 2015), and 7–100 mbar of sequestered volatilizable CO_2 (Bierson et al., 2016; Buhler & Piqueux, 2021). It has been debated for decades whether or not humans should warm Mars for the purposes of human habitation, with arguments both for (McKay, 1990) and against (Marshall, 1993). If we decide in the future to modify Mars' environment (Sagan, 1973), there is consensus that warming Mars by >30 K would be needed for seasonal meltwater (e.g., Averner & MacElroy, 1976; Graham, 2004; Marinova et al., 2005; McKay et al., 1991; Pollack & Sagan, 1993); an up-to-date review is DeBenedictis et al. (2025). While such warming long seemed impractical (Jakosky & Edwards, 2018), recent developments suggest new Mars-warming methods (e.g., Wordsworth et al., 2019), including release of IR-active particles (Ansari et al., 2024). However, prior work on warming with IR-active particles assumed static aerosol distributions based on natural dust aerosol distribution (Ansari et al., 2024) rather than modeling the dynamical behavior of engineered aerosol.

Aerosols are an important radiative agent in planetary atmospheres (Kahre et al., 2017; Yung & DeMore, 1999). Previous studies have examined aerosol feedbacks on Mars for natural particles, from local "solar escalator" effects (Batterson et al., 2023; Daerden et al., 2015; Spiga et al., 2013) to larger scales (e.g., Gebhardt et al., 2021; Kahre et al., 2015; Murphy et al., 1993; Newman et al., 2002; Rafkin, 2009; Urata et al., 2025; Wilson & Hamilton, 1996) and on Earth for smoke, volcanic ash, and other applications (De Laat et al., 2012; Gao et al., 2021; Khaykin et al., 2020; Ohneiser et al., 2023; Visioni et al., 2020; Yu et al., 2019). However, the

engineered aerosols considered for warming Mars have (by design) much stronger interaction with thermal-IR emission than with sunlight, whereas previous work has focused on self-lofting driven by absorption of sunlight. Ansari et al. (2024) considered IR-active particles but assumed a static particle distribution. Given that radiative-dynamical feedbacks (RDF) will be strong for IR-active particles released from Mars' surface, key atmospheric-dynamics questions remain: How high are aerosols lofted? How widely do they disperse? How do they couple with atmospheric circulation locally and globally? How long until steady state is reached? Does release location matter? Any Mars-warming method would face problems of manufacturing and environmental impact (e.g., both potential impact on humans and/or introduced plant life, and on, e.g., planetary climate via albedo changes) as well, but the radiative-dynamical questions must be addressed first. To this end, we added radiatively active engineered nanoparticle tracking to the Mars Weather Research and Forecasting (MarsWRF) code (Richardson et al., 2007; Toigo et al., 2012), building on previous work tracking methane plumes (Luo et al., 2021; Mischna et al., 2011) (Section 2). We specifically focus in this initial study on the simplest case of non-coagulating particles in a dry atmosphere released from a single, continuous source. This is done to minimize process complexity for this initial study and is not due to limitations with the model. More complex modeling will be necessary in the future to more completely address realistic release scenarios, particulate microphysical behavior, and climate physics. Instead, this study provides the necessary next step from idealized and/or 1D work that has been undertaken so far and provides a reference baseline for interpretation of future, more complex simulations.

2. Methods

We carry out separate numerical experiments that each consider one of two particle types for Mars warming: carbon (graphene disks) and metal (Al rods). Both target Mars' thermal infrared (TIR) windows at ∼10 and ∼20 μm via different mechanisms. Few-hundred-nm diameter graphene disks resonantly absorb TIR (Fang et al., 2014). To cover both spectral windows (Figure S3 in Supporting Information S1), in the graphene trials we used 16 parts (by number) 250 nm diameter disks to one part 1,000 nm diameter disks. Graphene is translucent to visible light, though it requires potentially costly modification for optimal performance (Supporting Information S1). Here, we adjust the electronic properties of the simulated graphene to give resonance height and width similar to Al rods. This implicitly assumes graphene is modified ("doped") to increase the carrier concentration (Supporting Information S1). The Al rods (60 nm-diameter, 8 μm long, one-eighth the weight of the particles considered in Ansari et al., 2024) both absorb and scatter thermal IR (Forget & Pierrehumbert, 1997). Either or both particle types might require anti-stick coatings, which are not modeled here. The goal is to examine plausible particles that might be produced: the chosen particles are not optimized for warming. As such, this study yields potentially realistic heating. It does not represent an upper limit on heating.

In our 3D (MarsWRF) modeling, we simulated continuous near-surface release of IR-active particles at both a northern-hemisphere midlatitude site (202°E 40°N, Arcadia Planitia), and separately at an equatorial site (135°E 0°N, Elysium Planitia), expressing release rate in liters/second (L/s) of solid aerosol (ranging from 0 to 60 L/s, Table S3 in Supporting Information S1). Particles can settle at the surface and we do not include any re-lofting mechanism. For natural dust, we imposed a time-varying background of radiatively active natural dust derived from an observational database (Montabone et al., 2015) for Mars Year 30, corresponding to a relatively storm-free scenario. The vertical distribution was further adjusted to that observed by Mars Climate Sounder (Kleinböhl et al., 2024). Dust was not allowed to interact with the engineered particles. Particle agglomeration is not included in the model, which is a significant limitation (Section 4). Gravitational settling speeds are obtained from analytical free molecular calculations for the appropriate shapes (Supporting Information S1). We also set the dry deposition velocity in the lowermost model layer, which is ∼9 m thick, to a minimum of 0.03 cm/s, to represent the effect of diffusive removal of small particles (Supporting Information S1). For comparison, the empirical exponential decay timescale for natural dust optical depth is ∼50 sols (Kahre et al., 2017).

We also used a 1D radiative-convective equilibrium model with Mars-average insolation (e.g., Ramirez, 2017) and a Single Column Model (SCM) version of WRF as a cross-check on warming. Results are shown in Figures S14 and S15, Table S4 in Supporting Information S1. The warming in 1D and 3D models differ (as do baseline global temperatures with no nanoparticle opacity), even when the same radiative transfer scheme is used (WRF SCM vs. GCM). The differences can be traced to differences in the vertical temperature profiles (and specifically temperature assumptions at the tropopause), the spectral resolution for radiative transfer, and the treatment of the atmosphere as a 3D system (see Supporting Information S1).

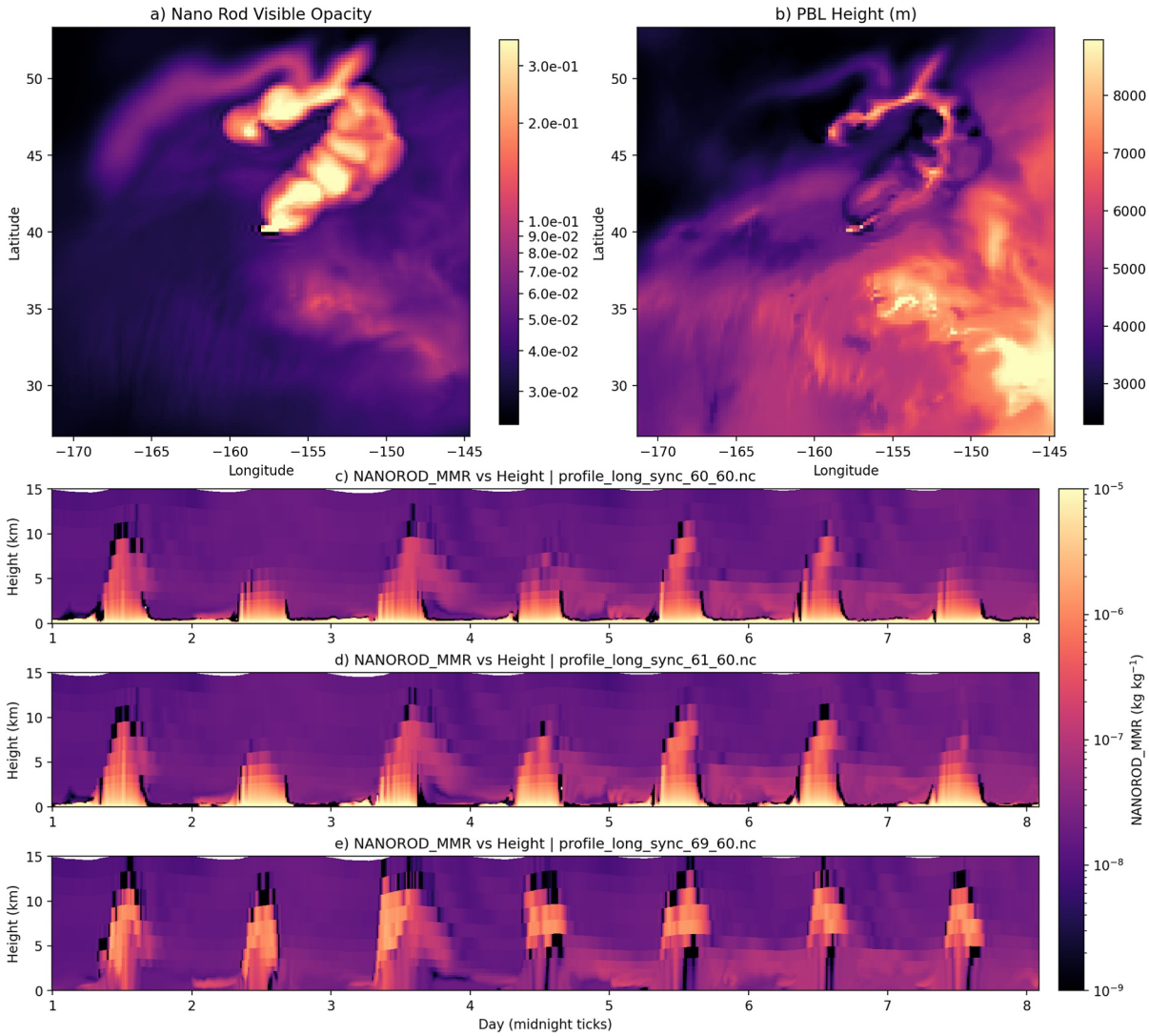

Figure 1. Local plume dynamics during initial deployment of 60 nm diameter Al rods at 60 L/s. Results are captured ∼6 sols from the time the plume is initiated. (a) Column-integrated opacity of particle plume at wavelength = 0.67 μm (τ_{vis}, unitless). (b) Planetary boundary layer (PBL) height (m). Both panels are for the same timestep, with a true local solar time of 11 a.m. at the source site. A mix of shadowing of the ground by plume particles and radiative heating of plume particles leads to a mixture of PBL suppression and augmentation in different locations. (c–e) Time-height cross-sections of plume mass mixing ratio in the lowest 10 km. Panel (c) is centered over the plume release site, (d) is one grid point (∼10 km) to the east, and (e) is ∼100 km further east. Nighttime accumulation in the stable surface layer is evident as a lighter color/yellow band; daytime convection ventilates the accumulated particles deep into the atmosphere, which can then advect downwind in the free atmosphere. Results are for release at Arcadia Planitia (202°E 40°N). MarsWRF has been set up to nest from 2° × 2° GCM domain, with two levels of nesting. The nested domain shown has 120 × 120 grid points and a grid spacing of 0.222°, corresponding to less than 13 km.

3. Results

High-spatial-resolution simulations show RDF during the initial release of IR-active particles in a nested version of MarsWRF. Figure 1 shows results for release from the midlatitude site for 60 nm diameter Al rods at a rate of 60 L/s. The plume self-lofts and thickens the Planetary Boundary Layer (PBL) height (Figures 1a and 1b show column visible opacity and PBL height at 11 a.m. local time at the release site), which is ∼2× thicker than without self-lofting (Figure S7 in Supporting Information S1). Above the release point (Figure 1c and top row), particles accumulate in the nighttime PBL before mixing upward during daytime. In adjacent grid boxes (Figure 1c, middle row), particles mix across the surface layer during late night and predawn, while early evening winds leave this region particle-free. Several grid points downwind (Figure 1c, bottom row), a detached high "anvil" of particles dominates the nanoparticle mass mixing ratio (mmr) between 5 and 10 km above the surface. Further from the plume (Figure S7 in Supporting Information S1), the particle mmr peaks between about 7.5 and 12.5 km, at or

above the top of the plume-free PBL. The vertical distribution of particles evolves as follows. While initially depleted at altitude, within 100 days an aerosol-enriched layer forms above 7 km. During southern spring, the strong Hadley cell temporarily halts particle buildup (Figure S6 in Supporting Information S1). These vertical variations diminish to 10% over years as mixing homogenizes the atmosphere. The steady-state particle distribution shows only a modest longitudinal enhancement (15° full-width-at-half-maximum) centered on the release site. Particle optical depth in steady state varies seasonally by 15%–20%, rising during northern summer when winds are weakest, regardless of release location.

Figures 2a–2f shows the global spread of nanoparticle mmr in lower resolution simulations (5° × 5°), for release at an equatorial site. The lower resolution is used to allow many more simulations to be undertaken than is possible for nested cases (such as for Figure 1). The high resolution allows more detail to be seen in the plume distribution but does not change the main results. The warming plume spreads eastward at all altitudes and also westward at high altitude in the high latitudes, with inter-hemispheric mixing occurring within months. These particles achieve warming much more efficiently than previous designs—a visible optical depth (τ_{vis}) of 0.2 requires only ∼33 mg/m^2 of aluminum rods in the aluminum simulations, and the same optical depth requires just over ∼17.5 mg/m^2 of graphene in the graphene simulations. The particles are more than twice as radiatively effective (in the thermal IR, per unit mass) than previous designs. The warming atmosphere inflates both in the sense of vertical expansion due directly to increased scale height, but also due to reduction in total mass of the seasonal CO_2 ice caps, see Table S3 in Supporting Information S1. This inflation combined with the RDF self-lofting lifts the suspended particles high into the atmosphere. The system approaches steady state with an e-folding timescale of ∼1.1 Mars years (Figure 3, Figure S8 in Supporting Information S1). The total time to achieve warming is about the same as the particle atmospheric lifetime. Cooling after particle release ends follows the same timescale. This timescale emerges from the model as the timescale for mixing any aerosol with similar radiative properties. Nothing has been done to make the particles mix more rapidly.

Figure 2d shows warm season surface temperatures. The warm season surface temperature is defined as the average surface temperature during the warmest 36° of solar longitude (∼70 days) of the year. This corresponds to southern summer in the southern ground ice zone, and northern summer in the northern ground ice zone.

The warmed climate develops a stronger meridional overturning circulation (Figure 4). The Hadley cells strengthen by a factor of 4 and shift upwards while the seasonal strength asymmetry (Richardson & Wilson, 2002) largely disappears. Because the particles are relatively well mixed in steady state, the mass streamfunction corresponds to the meridional overturning circulation of particles. Near-surface winds increase by 60% (global and annual average). Steeper temperature gradients develop between sunlit regions and the winter pole. This is the opposite of Earth's CO_2-warming response, which preferentially warms the poles and weakens circulation (Xia et al., 2020).

Surface pressure increases as seasonal CO_2 seasonal ice caps shrink. We do not consider release of additional CO_2 from perennial CO_2 ice nor from adsorbed regolith reservoirs, which would at least double the atmospheric pressure under warming (Bierson et al., 2016; Buhler & Piqueux, 2021). This thicker CO_2 atmosphere would add to the greenhouse effect, moderate the equator-pole temperature gradient, and expand the percentage of surface area above the triple point of water (Dickson et al., 2023).

The IR-active aerosols spread broadly, unlike patchy dust storms on Earth and Mars, because they settle very slowly. When artificially ballasted to give a settling speed corresponding to the diameter of natural Mars dust (3 μm), the particles produce strong concentration gradients—column depth varies by 5× between the release latitude and south pole, and particles remain below 200 Pa altitude. This creates localized warming, with a 2,000 km-wide +10 K warming zone, though less efficiently than global warming.

Among the two release sites tested, steady-state temperature is modestly warmer for equatorial release (Figure S9 in Supporting Information S1), with greater temperature differences for higher particle loads. The steady-state particle loading is also slightly higher, as expected given the longer distances (and correspondingly longer time for sedimentation) for particles released from a far northern site to spread globally.

4. Discussion

For the first time, we modeled the atmospheric dynamics of IR-active particles released from Mars' surface in a global 3D model. Further research is needed on both Mars and warming options before committing to any plan for

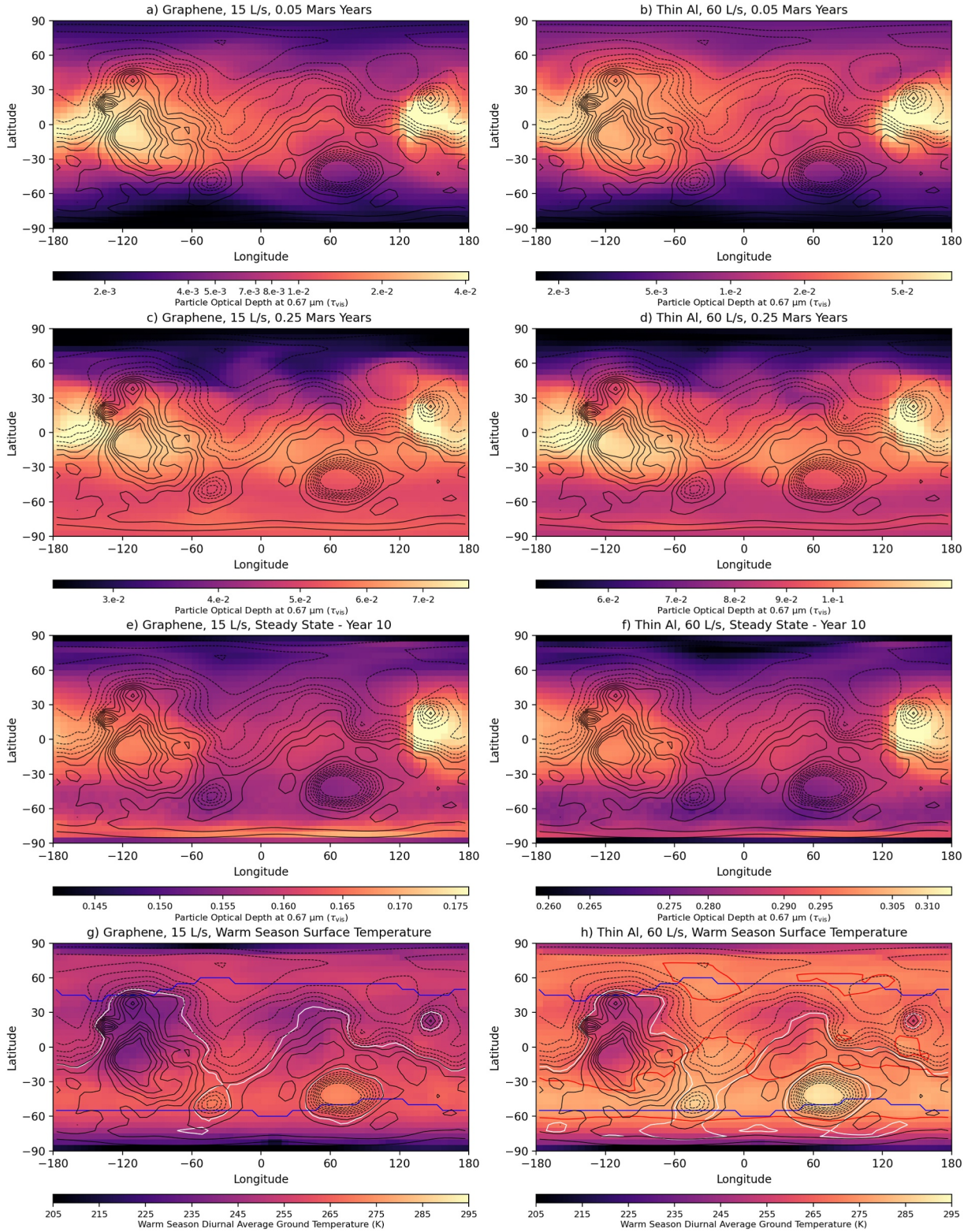

Figure 2. Dynamics of particle spread and steady-state global warming. Left: 15 L/s carbon (graphene) disks (*run Cc41*). Right: 60 L/s metal rods (*run Cc16*). Both assuming 0°N 135°E release. (a–f) Particle optical depth at 0.67 μm (τ_{vis}). (g, h) Filled color: warm season temperatures (K). Black topographic contours correspond to elevations of −5 and −2 km (dashed), and 0, +2, and +5 km (solid). White contour: 610 Pa (~6 mbar) mean pressure level. Blue contour: Approximate equatorward extent of H_2O ice at <1 m depth based on GRS data (Feldman et al., 2004). Red contour: Highlights warm-season average surface temperatures above 273 K.

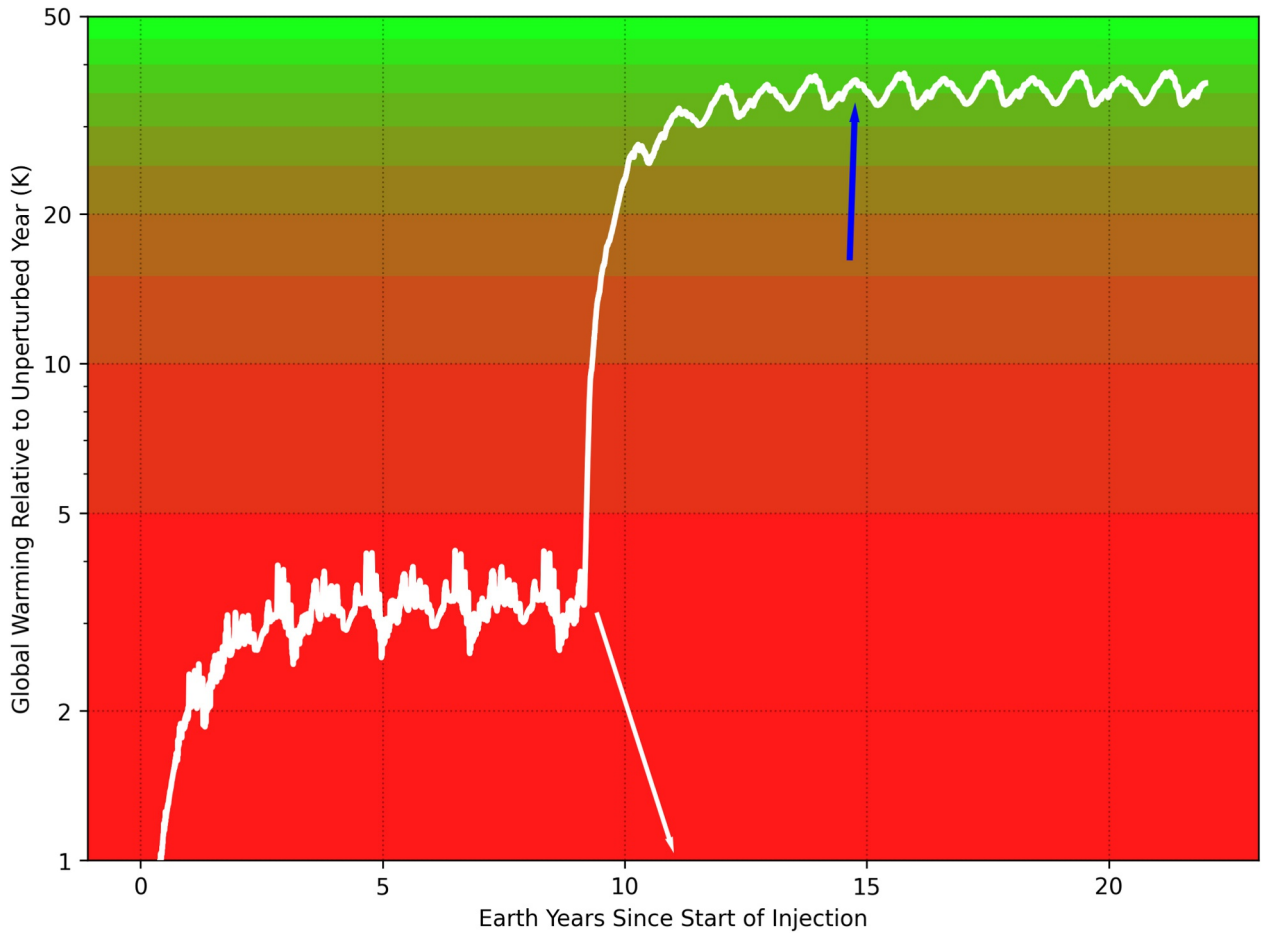

Figure 3. Time evolution of global average surface temperature, assuming a 3 L/s IR-active particle release starting at the northern equinox for the first 5 Mars years (just over 9 Earth years), followed by increase to 60 L/s. Al particles assumed. These two different rates show that the response timescale is almost independent of the release rate. After 8 Mars years (15 Earth-yr, indicated by blue arrow), the average warm-season temperature at 47.5°S exceeds 280 K. The line is constructed by taking the daily global average surface temperature and removing from it the global average temperature for the same day-of-year (sol) from the steady-state reference run. Note that net warming is a modest function of season due to the distribution of nanoparticles. If a choice is made to cease warming, then the planet rapidly cools to the no-warming state (roughly following the white arrow to zero warming).

Mars' future (DeBenedictis et al., 2025). For example, the case for maintaining Mars' surface as a pristine wilderness indefinitely is given in Marshall (1993). Moreover, making Mars' surface suitable for life involves many steps beyond initial warming, for example, soil chemistry and suitability for biology (DeBenedictis et al., 2025). Progress here would be useful for both investigations of Mars' possible future habitability and for astrobiology research (Wordsworth & Cockell, 2024; Wordsworth et al., 2025).

As warmer climates have more water vapor, and water vapor is a greenhouse gas, water vapor feedback will strengthen warming. Water ice clouds have also been proposed to provide strong positive feedback for Mars warming (e.g., Madeleine et al., 2014; Wilson et al., 2008), although this depends on grain size and cloud height. As the water cycle intensifies, aerosol may act as ice nuclei/cloud condensation nuclei, which may scavenge aerosol. Even if snow does not reach the ground, scavenging can still transport aerosol vertically downward prior to sublimation (i.e., virga). These examples show that water cycle feedbacks require further study. Additionally, a more active water cycle within a circulation that has enhanced "dust storm-like" global circulation (Figure 4d) will likely greatly increase water atmospheric loss rates to space (Chaffin et al., 2021; Heavens et al., 2018) above the current rate of approximately 0.005% of Mars' confirmed water inventory per million years.

Several unmodeled dust feedbacks are potentially important. Initially, stronger surface winds would lift more dust (Hartwick et al., 2022), creating a potential negative feedback since dust reduces dayside temperatures despite causing net warming (Streeter et al., 2020). However, strong warming would eliminate the CO_2 ice cap edge

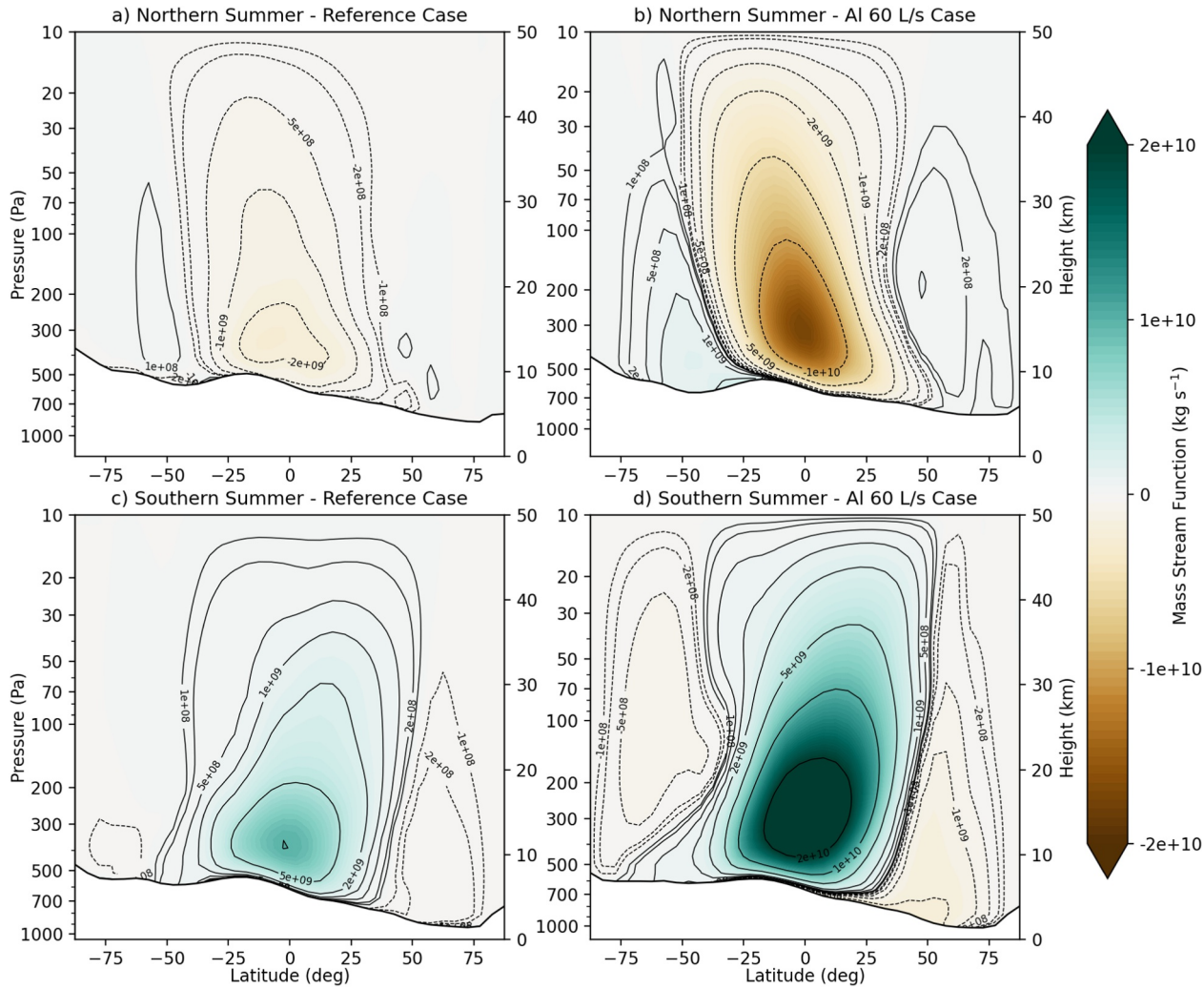

Figure 4. Atmospheric circulation strengthens under aerosol warming. Streamfunctions (kg/s) for (a, c) control and (b, d) 60 L/s Al-particle warming cases. (a, b) Northern summer, (c, d) southern summer. Positive values: clockwise mass flux (looking toward the west). The surface pressure changes due to the reduction in seasonal CO_2 ice in the warmed case. Note that the plot is limited to 50 km to focus on the lower-to-mid tropospheric circulation, but the model top is at roughly 100 km.

where strong dust lifting generates most Martian dust storms (Kahre et al., 2017). Additionally, dust can be trapped both by surface liquid water and in high-altitude "duststones" (Bridges & Muhs, 2012).

Aerosol-aerosol and aerosol-surface interactions warrant further research. Agglomeration of particles (Bertrand et al., 2022) is most likely during dispersal. Scavenging by condensation of water onto the engineered aerosol could remove a significant fraction of the particles. Possible mitigations include anti-stick coatings, more dispersal points, charging, and day-only release. Since coatings can be very thin (atomic scale), they need not matter much for radiative properties. Agglomerates are deliberately produced during aerosol synthesis (and their properties tuned) (Buesser & Pratsinis, 2012; Friedlander, 2000), and it is possible that agglomerates will remain both efficient at Mars warming and also easily wind-transported, depending on their fractal dimension. Agglomeration between engineered aerosols and natural dust might also occur. Few data exist regarding dry deposition of submicron particles on desert surfaces, and this uncertainty is important (e.g., Emerson et al., 2020; Li et al., 2025; Zhang & Shao, 2014). If the dry deposition rate is 3× greater, then the particle lifetime will be 3× shorter for slow-settling particles such as graphene disks.

Particles must be engineered to break down in the natural environment. Methods include adding spacers, designing for water solubility, further thinning for oxidation frangibility, and functionalization. Graphene particles could offer additional benefits if doped with soil nutrients. In our simulations, even though Mars' low-

latitude temperature swings are reduced, they remain ∼100 K, and winter-minimum temperatures in the ground-ice-rich latitudes remain cold (<230 K for latitudes poleward of 30°). These swings will moderate as Mars' atmospheric thickness further increases but will remain severe by Earth standards.

Other particle release strategies might lead to stronger warming than the continuous and steady one used here. For example, particles could be released during the season when the circulation at the site is upward, or at locations and times that have strong diurnal updrafts.

We note that although self-lofting helps particles rise and spread for initial deployment (Figure 1 and Figure S7 in Supporting Information S1), and we run to steady state, we have not determined whether the self-lofting is important in maintaining, as opposed to establishing, the steady-state warmed atmosphere.

Either carbon or metal particles could warm Mars from near-surface release, if produced at scale. The details of how particles are prepared with both high throughput and sufficient uniformity are challenging (Supporting Information S1).

Analyzing Mars with stronger longwave forcing but the same orbital forcing is scientifically interesting, especially as comparison to Mars' geologically recent past, with similar longwave forcing but different orbital forcing, is a major scientific goal (MEPAG, 2025).

5. Conclusions

Using a particle-tracking climate model, we simulated the atmospheric dynamics of warming Mars with engineered aerosol. We find that RDF, including local self-lofting and stronger large-scale circulation, aids particle spread. This study addresses only some aspects of the question of IR-active particle release might modify Mars' climate: atmospheric processes are inherently complex, and many open questions remain. These include water cycle feedbacks and agglomeration mitigation approaches.

Conflict of Interest

The authors declare no conflicts of interest relevant to this study.

Availability Statement

Model output corresponding to the figures shown is available, see Richardson and Kite (2025). FDTD: 3D Electromagnetic Simulator is commercial code (Lumerical). The MarsWRF source code can be made available by Aeolis Research pending scientific review and a completed Rules of the Road agreement. Requests for the MarsWRF source code should be submitted to mir@aeolisresearch.com.

Acknowledgments
We thank C. Willard, A.S. Braude, M. Wang, M. Hersam, R. Zubrin, N. Myrhvold, D. Keith, C. Lee, A.P. Raman, M. Mester, and the PlanetWRF development team. This work used GrADS (COLA/IGES). This work used resources from the University of Chicago's Research Computing Center. Part of the resources supporting this work were provided by the NASA High-End Computing (HEC) Program through the NASA Advanced Supercomputing (NAS) Division at Ames Research Center. This research was supported in part through the computational resources and staff contributions provided for the Quest high performance computing facility at Northwestern University which is jointly supported by the Office of the Provost, the Office for Research, and Northwestern University Information Technology. A portion of this work was conducted at the Jet Propulsion Laboratory, California Institute of Technology, under a contract with NASA.

References

Ansari, S., Kite, E. S., Ramirez, R., Steele, L. J., & Mohseni, H. (2024). Feasibility of keeping Mars warm with nanoparticles. *Science Advances*, *10*(32), eadn4650. https://doi.org/10.1126/sciadv.adn4650

Averner, M. M., & MacElroy, R. D. (1976). On the habitability of Mars: An approach to planetary ecosynthesis (NASA-SP-414).

Batterson, C. M., Kahre, M. A., Bridger, A. F., Wilson, R. J., Urata, R. A., & Bertrand, T. (2023). Modeling the "B" regional dust storm on Mars: Dust lofting mechanisms predicted by the new NASA Ames Mars GCM. *Icarus*, *400*, 115542. https://doi.org/10.1016/j.icarus.2023.115542

Bertrand, T., Kahre, M. A., Urata, R., Määttänen, A., Montmessin, F., Wilson, R. J., & Wolff, M. J. (2022). Impact of the coagulation of dust particles on Mars during the 2018 global dust storm. *Icarus*, *388*, 115239. https://doi.org/10.1016/j.icarus.2022.115239

Bierson, C. J., Phillips, R. J., Smith, I. B., Wood, S. E., Putzig, N. E., Nunes, D., & Byrne, S. (2016). Stratigraphy and evolution of the buried CO_2 deposit in the Martian south polar cap. *Geophysical Research Letters*, *43*(9), 4172–4179. https://doi.org/10.1002/2016GL068457

Bridges, N. T., & Muhs, D. R. (2012). Duststones on Mars: Source, transport, deposition, and erosion. In J. Grotzinger & R. Milliken (Eds.), *Sedimentary geology of Mars* (Vol. 102). SEPM Special Publication.

Buesser, B., & Pratsinis, S. E. (2012). Design of nanomaterial synthesis by aerosol processes. *Annual Review of Chemical and Biomolecular Engineering*, *3*(1), 103–127. https://doi.org/10.1146/annurev-chembioeng-062011-080930

Buhler, P. B., & Piqueux, S. (2021). Obliquity-driven CO_2 exchange between Mars' atmosphere, regolith, and polar cap. *Journal of Geophysical Research: Planets*, *126*(5), e2020JE006759. https://doi.org/10.1029/2020JE006759

Carr, M. H., & Head, J. W. (2015). Martian surface/near-surface water inventory: Sources, sinks, and changes with time. *Geophysical Research Letters*, *42*(3), 726–732. https://doi.org/10.1002/2014GL062464

Chaffin, M. S., Kass, D. M., Aoki, S., Fedorova, A. A., Deighan, J., Connour, K., et al. (2021). Martian water loss to space enhanced by regional dust storms. *Nature Astronomy*, *5*(10), 1036–1042. https://doi.org/10.1038/s41550-021-01425-w

Daerden, F., Whiteway, J. A., Neary, L., Komguem, L., Lemmon, M. T., Heavens, N. G., et al. (2015). A solar escalator on Mars: Self-lifting of dust layers by radiative heating. *Geophysical Research Letters*, *42*(18), 7319–7326. https://doi.org/10.1002/2015GL064892

DeBenedictis, E. A., Kite, E. S., Wordsworth, R. D., Lanza, N. L., Cockell, C. S., Silver, P. A., et al. (2025). The case for Mars terraforming research. *Nature Astronomy*, *9*(5), 634–639. https://doi.org/10.1038/s41550-025-02548-0

De Laat, A. T. J., Stein Zweers, D. C., Boers, R., & Tuinder, O. N. (2012). A solar escalator: Observational evidence of the self-lifting of smoke and aerosols by absorption of solar radiation in the February 2009 Australian Black Saturday plume. *Journal of Geophysical Research*, *117*(D4). https://doi.org/10.1029/2011JD017016

Dickson, J. L., Palumbo, A. M., Head, J. W., Kerber, L., Fassett, C. I., & Kreslavsky, M. A. (2023). Gullies on Mars could have formed by melting of water ice during periods of high obliquity. *Science*, *380*(6652), 1363–1367. https://doi.org/10.1126/science.abk2464

Emerson, E. W., Hodshire, A. L., DeBolt, H. M., Bilsback, K. R., Pierce, J. R., McMeeking, G. R., & Farmer, D. K. (2020). Revisiting particle dry deposition and its role in radiative effect estimates. *Proceedings of the National Academy of Sciences*, *117*(42), 26076–26082. https://doi.org/10.1073/pnas.2014761117

Fang, Z., Wang, Y., Schlather, A. E., Liu, Z., Ajayan, P. M., García de Abajo, F. J., et al. (2014). Active tunable absorption enhancement with graphene nanodisk arrays. *Nano Letters*, *14*(1), 299–304. https://doi.org/10.1021/nl404042h

Feldman, W. C., Prettyman, T. H., Maurice, S., Plaut, J. J., Bish, D. L., Vaniman, D. T., et al. (2004). Global distribution of near-surface hydrogen on Mars. *Journal of Geophysical Research*, *109*(E9), E09006. https://doi.org/10.1029/2003je002160

Forget, F., & Pierrehumbert, R. T. (1997). Warming early Mars with carbon dioxide clouds that scatter infrared radiation. *Science*, *278*(5341), 1273–1276. https://doi.org/10.1126/science.278.5341.1273

Friedlander, S. K. (2000). *Smoke, dust, and haze* (2nd ed.). Oxford University Press.

Gao, R. S., Rosenlof, K. H., Kärcher, B., Tilmes, S., Toon, O. B., Maloney, C., & Yu, P. (2021). Toward practical stratospheric aerosol albedo modification: Solar-powered lofting. *Science Advances*, *7*(20), eabe3416. https://doi.org/10.1126/sciadv.abe3416

Gebhardt, C., Abuelgasim, A., Fonseca, R. M., Martín-Torres, J., & Zorzano, M. P. (2021). Characterizing dust-radiation feedback and refining the horizontal resolution of the MarsWRF model down to 0.5 degree. *Journal of Geophysical Research: Planets*, *126*(3), e2020JE006672. https://doi.org/10.1029/2020JE006672

Graham, J. M. (2004). The biological terraforming of Mars: Planetary ecosynthesis as ecological succession on a global scale. *Astrobiology*, *4*(2), 168–195. https://doi.org/10.1089/153110704323175133

Hartwick, V. L., Haberle, R. M., Kahre, M. A., & Wilson, R. J. (2022). The dust cycle on Mars at different orbital distances from the Sun: An investigation of the impact of radiatively active dust on land planet climate. *The Astrophysical Journal*, *941*(1), 54. https://doi.org/10.3847/1538-4357/ac9481

Heavens, N. G., Kleinböhl, A., Chaffin, M. S., Halekas, J. S., Kass, D. M., Hayne, P. O., et al. (2018). Hydrogen escape from Mars enhanced by deep convection in dust storms. *Nature Astronomy*, *2*, 126–132. https://doi.org/10.1038/s41550-017-0353-4

Jakosky, B. M., & Edwards, C. S. (2018). Inventory of CO_2 available for terraforming Mars. *Nature Astronomy*, *2*(8), 634–639. https://doi.org/10.1038/s41550-018-0529-6

Kahre, M. A., Hollingsworth, J. L., Haberle, R. M., & Wilson, R. J. (2015). Coupling the Mars dust and water cycles: The importance of radiative-dynamic feedbacks during northern hemisphere summer. *Icarus*, *260*, 477–480. https://doi.org/10.1016/j.icarus.2014.07.017

Kahre, M. A., Murphy, J. R., Newman, C. E., Wilson, R. J., Cantor, B. A., Lemmon, M. T., & Wolff, M. J. (2017). The Mars dust cycle. In R. Haberle, R. T. Clancy, F. Forget, M. D. Smith, & R. W. Zurek (Eds.), *The atmosphere and climate of Mars* (p. 295). Cambridge University Press.

Khaykin, S., Legras, B., Bucci, S., Sellitto, P., Isaksen, L., Tencé, F., et al. (2020). The 2019/20 Australian wildfires generated a persistent smoke-charged vortex rising up to 35 km altitude. *Communications Earth & Environment*, *1*(1), 22. https://doi.org/10.1038/s43247-020-00022-5

Kleinböhl, A., Kass, D. M., Schreier, M., Piqueux, S., Suzuki, S., Shirley, J. H., et al. (2024). Far infrared radiative properties of Mars atmospheric aerosols and their application to Mars Climate Sounder retrievals of aerosol profiles, aerosol columns and surface temperatures. *Icarus*, *419*, 116000. https://doi.org/10.1016/j.icarus.2024.116000

Li, L., Zhao, C., Newman, C. E., Zhao, Y., Feng, J., Li, T., et al. (2025). Impacts of dry deposition processes with resolved dust particle sizes on simulating the Martian dust. *Journal of Geophysical Research: Planets*, *130*(5), e2024JE008616. https://doi.org/10.1029/2024JE008616

Luo, Y., Mischna, M. A., Lin, J. C., Fasoli, B., Cai, X., & Yung, Y. L. (2021). Mars methane sources in northwestern Gale crater inferred from back trajectory modeling. *Earth and Space Science*, *8*(11), e2021EA001915. https://doi.org/10.1029/2021EA001915

Madeleine, J. B., Head, J. W., Forget, F., Navarro, T., Millour, E., Spiga, A., et al. (2014). Recent ice ages on Mars: The role of radiatively active clouds and cloud microphysics. *Geophysical Research Letters*, *41*(14), 4873–4879. https://doi.org/10.1002/2014GL059861

Marinova, M. M., McKay, C. P., & Hashimoto, H. (2005). Radiative-convective model of warming Mars with artificial greenhouse gases. *Journal of Geophysical Research*, *110*(E3). https://doi.org/10.1029/2004JE002306

Marshall, A. (1993). Ethics and the extraterrestrial environment. *Journal of Applied Philosophy*, *10*(2), 227–236. https://doi.org/10.1111/j.1468-5930.1993.tb00078.x

McKay, C. P. (1990). Does Mars have rights? An approach to the environmental ethics of planetary engineering. In D. McNiven (Ed.), *Moral expertise: Studies in practical and professional ethics* (pp. 184–197). Routledge.

McKay, C. P., Toon, O. B., & Kasting, J. F. (1991). Making Mars habitable. *Nature*, *352*(6335), 489–496. https://doi.org/10.1038/352489a0

MEPAG, Mars Scientific Goals. (2025). Objectives, investigations, and priorities. In D. Banfield (Ed.), *White paper posted September, 2025 by the Mars Exploration program Analysis Group (MEPAG)* (Vol. 78). Retrieved from https://www.lpi.usra.edu/mepag/goals/

Mischna, M. A., Allen, M., Richardson, M. I., Newman, C. E., & Toigo, A. D. (2011). Atmospheric modeling of Mars methane surface releases. *Planetary and Space Science*, *59*(2–3), 227–237. https://doi.org/10.1016/j.pss.2010.07.005

Montabone, L., Forget, F., Millour, E., Wilson, R. J., Lewis, S. R., Cantor, B., et al. (2015). Eight-year climatology of dust optical depth on Mars. *Icarus*, *251*, 65–95. https://doi.org/10.1016/j.icarus.2014.12.034

Murphy, J. R., Haberle, R. M., Toon, O. B., & Pollack, J. B. (1993). Martian global dust storms: Zonally symmetric numerical simulations including size-dependent particle transport. *Journal of Geophysical Research*, *98*(E2), 3197–3220. https://doi.org/10.1029/92JE02945

Newman, C. E., Lewis, S. R., Read, P. L., & Forget, F. (2002). Modeling the Martian dust cycle 2. Multiannual radiatively active dust transport simulations. *Journal of Geophysical Research*, *107*(E12), 7-1. https://doi.org/10.1029/2002JE001920

Ohneiser, K., Ansmann, A., Witthuhn, J., Deneke, H., Chudnovsky, A., Walter, G., & Senf, F. (2023). Self-lofting of wildfire smoke in the troposphere and stratosphere: Simulations and space LiDAR observations. *Atmospheric Chemistry and Physics*, *23*(4), 2901–2925. https://doi.org/10.5194/acp-23-2901-2023

Pollack, J. B., & Sagan, C. (1993). Planetary engineering. In J. S. Lewis, M. S. Matthews, & M. L. Guerrieri (Eds.), *Resources of near-earth space* (pp. 921–950). University of Arizona Press.

Rafkin, S. C. (2009). A positive radiative-dynamic feedback mechanism for the maintenance and growth of Martian dust storms. *Journal of Geophysical Research*, *114*(E1). https://doi.org/10.1029/2008JE003217

Ramirez, R. M. (2017). A warmer and wetter solution for early Mars and the challenges with transient warming. *Icarus*, *297*, 71–82. https://doi.org/10.1016/j.icarus.2017.06.025
Richardson, M. I., & Kite, E. S. (2025). Supplementary data for "Atmospheric dynamics of first steps toward terraforming Mars", by Richardson et al [Dataset]. *Zenodo*. https://doi.org/10.5281/zenodo.17844025
Richardson, M. I., Toigo, A. D., & Newman, C. E. (2007). PlanetWRF: A general purpose, local to global numerical model for planetary atmospheric and climate dynamics. *Journal of Geophysical Research*, *112*(E9). https://doi.org/10.1029/2006JE002825
Richardson, M. I., & Wilson, R. J. (2002). A topographically forced asymmetry in the Martian circulation and climate. *Nature*, *416*(6878), 298–301. https://doi.org/10.1038/416298a
Sagan, C. (1973). Planetary engineering on Mars. *Icarus*, *20*(4), 513–514. https://doi.org/10.1016/0019-1035(73)90026-2
Spiga, A., Faure, J., Madeleine, J. B., Määttänen, A., & Forget, F. (2013). Rocket dust storms and detached dust layers in the Martian atmosphere. *Journal of Geophysical Research: Planets*, *118*(4), 746–767. https://doi.org/10.1002/jgre.20046
Streeter, P. M., Lewis, S. R., Patel, M. R., Holmes, J. A., & Kass, D. M. (2020). Surface warming during the 2018/Mars year 34 global dust storm. *Geophysical Research Letters*, *47*(9), e2019GL083936. https://doi.org/10.1029/2019GL083936
Toigo, A. D., Lee, C., Newman, C. E., & Richardson, M. I. (2012). The impact of resolution on the dynamics of the Martian global atmosphere: Varying resolution studies with the MarsWRF GCM. *Icarus*, *221*(1), 276–288. https://doi.org/10.1016/j.icarus.2012.07.020
Urata, R. A., Bertrand, T., Kahre, M. A., Wilson, R. J., Kling, A. M., & Wolff, M. (2025). Impact of a bimodal dust distribution on the 2018 Martian global dust storm with the NASA Ames Mars global climate model. *Icarus*, *429*, 116446. https://doi.org/10.1016/j.icarus.2024.116446
Visioni, D., MacMartin, D. G., Kravitz, B., Lee, W., Simpson, I. R., & Richter, J. H. (2020). Reduced poleward transport due to stratospheric heating under stratospheric aerosols geoengineering. *Geophysical Research Letters*, *47*(17), e2020GL089470. https://doi.org/10.1029/2020GL089470
Wilson, R. J., & Hamilton, K. (1996). Comprehensive model simulation of thermal tides in the Martian atmosphere. *Journal of the Atmospheric Sciences*, *53*(9), 1290–1326. https://doi.org/10.1175/1520-0469(1996)053<1290:CMSOTT>2.0.CO;2
Wilson, R. J., Lewis, S. R., Montabone, L., & Smith, M. D. (2008). Influence of water ice clouds on Martian tropical atmospheric temperatures. *Geophysical Research Letters*, *35*(7), L07202. https://doi.org/10.1029/2007GL032405
Wordsworth, R., Cherubim, C., Nangle, S., Berliner, A., Dyson, E., Girguis, P., et al. (2025). Applied astrobiology: An integrated approach to the future of life in space. *Astrobiology*, *25*(5), 327–330. https://doi.org/10.1089/ast.2024.0156
Wordsworth, R., & Cockell, C. (2024). Self-sustaining living habitats in extraterrestrial environments. *Astrobiology*, *24*(12), 1187–1195. https://doi.org/10.1089/ast.2024.0080
Wordsworth, R., Kerber, L., & Cockell, C. (2019). Enabling Martian habitability with silica aerogel via the solid-state greenhouse effect. *Nature Astronomy*, *3*(10), 898–903. https://doi.org/10.1038/s41550-019-0813-0
Xia, Y., Hu, Y., & Liu, J. (2020). Comparison of trends in the Hadley circulation between CMIP6 and CMIP5. *Science Bulletin*, *65*(19), 1667–1674. https://doi.org/10.1016/j.scib.2020.06.011
Yu, P., Toon, O. B., Bardeen, C. G., Zhu, Y., Rosenlof, K. H., Portmann, R. W., et al. (2019). Black carbon lofts wildfire smoke high into the stratosphere to form a persistent plume. *Science*, *365*(6453), 587–590. https://doi.org/10.1126/science.aax1748
Yung, Y. L., & DeMore, W. B. (1999). *Photochemistry of planetary atmospheres*. Oxford University Press.
Zhang, J., & Shao, Y. (2014). A new parameterization of particle dry deposition over rough surfaces. *Atmospheric Chemistry and Physics*, *14*(22), 12429–12440. https://doi.org/10.5194/acp-14-12429-2014

References From the Supporting Information

Deokar, G., Jin, J., Schwingenschlögl, U., Kanoun, M. B., & Costa, P. M. F. J. (2022). Chemical vapor deposition-grown nitrogen-doped graphene's synthesis, characterization and applications. *npj 2D Materials and Applications*, *6*(1), 14. https://doi.org/10.1038/s41699-022-00287-8
Fang, Z., Thongrattanasiri, S., Schlather, A., Liu, Z., Ma, L., Wang, Y., et al. (2013). Gated tunability and hybridization of localized plasmons in nanostructured graphene. *ACS Nano*, *7*(3), 2388–2395. https://doi.org/10.1021/nn3055835
Grebenko, A. K., Krasnikov, D. V., Bubis, A. V., Stolyarov, V. S., Vyalikh, D. V., Makarova, A. A., et al. (2022). High-quality graphene using Boudouard reaction. *Advanced Science*, *9*(12), 2200217. https://doi.org/10.1002/advs.202200217
Guo, B., Fang, L., Zhang, B., & Gong, J. R. (2011). Graphene doping: A review. *Insciences Journal*, *1*(2), 80–89. https://doi.org/10.5640/insc.010280
Haberle, R. M. (2013). Estimating the power of Mars' greenhouse effect. *Icarus*, *223*(1), 619–620. https://doi.org/10.1016/j.icarus.2012.12.022
Haberle, R. M., Clancy, R. T., Forget, F., Smith, M. D., & Zurek, R. W. (Eds.) (2017). *The atmosphere and climate of Mars*. Cambridge University Press.
Haberle, R. M., Kahre, M. A., Bertrand, T., & Wolff, M. J. (2025). Modeling studies of dust/gas non-thermal equilibrium in the Martian atmosphere. *Icarus*, *429*, 116452. https://doi.org/10.1016/j.icarus.2024.116452
Hartwick, V. L., Toon, O. B., Lundquist, J. K., Pierpaoli, O. A., & Kahre, M. A. (2023). Assessment of wind energy resource potential for future human missions to Mars. *Nature Astronomy*, *7*(3), 298–308. https://doi.org/10.1038/s41550-022-01851-4
He, C., Jiang, S., & Shen, P. (2013). Large-scale and rapid synthesis of disk-shaped and nano-sized graphene. *Scientific Reports*, *3*(1), 2144. https://doi.org/10.1038/srep02144
Hinterman, E. D. (2022). *Multi-objective system optimization of a Mars atmospheric ISRU plant Doctoral dissertation*. Massachusetts Institute of Technology. Retrieved from https://hdl.handle.net/1721.1/145095
Hoffman, J. A., Hecht, M. H., Rapp, D., Hartvigsen, J. J., SooHoo, J. G., Aboobaker, A. M., et al. (2022). Mars Oxygen ISRU Experiment (MOXIE)—Preparing for human Mars exploration. *Science Advances*, *8*(35), eabp8636. https://doi.org/10.1126/sciadv.abp8636
Hong, S. Y., Noh, Y., & Dudhia, J. (2006). A new vertical diffusion package with an explicit treatment of entrainment processes. *Monthly Weather Review*, *134*(9), 2318–2341. https://doi.org/10.1175/MWR3199.1
Klimchitskaya, G. L., & Mostepanenko, V. M. (2013). Van der Waals and Casimir interactions between two graphene sheets. *Physical Review B: Condensed Matter and Materials Physics*, *87*(7), 075439. https://doi.org/10.1103/PhysRevB.87.075439
Liu, H., Liu, Y., & Zhu, D. (2010). Chemical doping of graphene. *Journal of Materials Chemistry*, *20*, 10928–10934.
Luong, D. X., Bets, K. V., Algozeeb, W. A., Stanford, M. G., Kittrell, C., Chen, W., et al. (2020). Gram-scale bottom-up flash graphene synthesis. *Nature*, *577*(7792), 647–651. https://doi.org/10.1038/s41586-020-1938-0
Manabe, S., & Wetherald, R. T. (1967). Thermal equilibrium of the atmosphere with a given distribution of relative humidity. *Journal of the Atmospheric Sciences*, *24*(3), 241–259. https://doi.org/10.1175/1520-0469(1967)024<0241:TEOTAW>2.0.CO;2

Mbayachi, V. B., Ndayiragije, E., Sammani, T., Taj, S., Mbuta, E. R., & Khan, A. U. (2021). Graphene synthesis, characterization and its applications: A review. *Results in Chemistry*, *3*, 100163. https://doi.org/10.1016/j.rechem.2021.100163

McClellan, J., Keith, D. W., & Apt, J. (2012). Cost analysis of stratospheric albedo modification delivery systems. *Environmental Research Letters*, *7*(3), 034019. https://doi.org/10.1088/1748-9326/7/3/034019

Mischna, M. A., Lee, C., & Richardson, M. (2012). Development of a fast, accurate radiative transfer model for the Martian atmosphere, past and present. *Journal of Geophysical Research*, *117*(E10). https://doi.org/10.1029/2012JE004110

Neto, A. H., Guinea, F., Peres, N. M. R., Novoselov, K. S., & Geim, A. K. (2009). The electronic properties of graphene. *Reviews of Modern Physics*, *81*(1), 109–162. https://doi.org/10.1103/RevModPhys.81.109

Paton, K. R., Varrla, E., Backes, C., Smith, R. J., Khan, U., O'Neill, A., et al. (2014). Scalable production of large quantities of defect-free few-layer graphene by shear exfoliation in liquids. *Nature Materials*, *13*(6), 624–630. https://doi.org/10.1038/nmat3944

Rakić, A. D. (1995). Algorithm for the determination of intrinsic optical constants of metal films: Application to aluminum. *Applied Optics*, *34*(22), 4755–4767. https://doi.org/10.1364/AO.34.004755

Ramirez, R. M., & Kasting, J. F. (2017). Could cirrus clouds have warmed early Mars? *Icarus*, *281*, 248–261. https://doi.org/10.1016/j.icarus.2016.08.016

Ramirez, R. M., Kopparapu, R., Zugger, M. E., Robinson, T. D., Freedman, R., & Kasting, J. F. (2014). Warming early Mars with CO_2 and H_2. *Nature Geoscience*, *7*(1), 59–63. https://doi.org/10.1038/ngeo2000

Rapp, D., & Hinterman, E. (2023). Adapting a Mars ISRU System to the changing Mars environment. *Space: Science & Technology*, *3*, 0041. https://doi.org/10.34133/space.0041

Sharipov, F. (2016). *Rarefied gas dynamics: Fundamentals for research and practice*. Wiley-VCH.

Romero-Guzman, C., Perez-Grande, I., & Rodriguez-Manfredi, J. A. (2023). Thermal model of InSight solar panels in Martian conditions. *Acta Astronautica*, *202*, 476–484. https://doi.org/10.1016/j.actaastro.2022.10.045

Stern, J. C., Malespin, C. A., Eigenbrode, J. L., Webster, C. R., Flesch, G., Franz, H. B., et al. (2022). Organic carbon concentrations in 3.5-billion-year-old lacustrine mudstones of Mars. *Proceedings of the National Academy of Sciences*, *119*(27), e2201139119. https://doi.org/10.1073/pnas.2201139119

Staley, J. T., & Haupin, W. (2000). Aluminum and aluminum alloys. In *Kirk-Othmer encyclopedia of chemical technology* (4th ed., volume 2). Kirk-Othmer.

Thekaekara, M. P. (1973). Solar energy outside the Earth's atmosphere. *Solar Energy*, *14*(2), 109–127. https://doi.org/10.1016/0038-092X(73)90028-5

Tikuišis, K. K., Dubroka, A., Uhlířová, K., Speck, F., Seyller, T., Losurdo, M., et al. (2023). Dielectric function of epitaxial quasi-freestanding monolayer graphene on Si-face 6H-SiC in a broad spectral range. *Physical Review Materials*, *7*(4), 044201. https://doi.org/10.1103/PhysRevMaterials.7.044201

Williams, R. J., McKay, D. S., Giles, D., & Bunch, T. E. (1979). Mining and beneficiation of lunar ores. In *Space resources and space settlements (NASA SP-428)* (pp. 275–288).

Wollman, M. J., & Zika, M. J. (2006). Prometheus project reactor module final report, for naval reactors information. https://doi.org/10.2172/884680

Geophysical Research Letters

Supporting Information for

Atmospheric dynamics of IR-active particles released from Mars' surface.

Mark I. Richardson[1,*], Samaneh Ansari[2], Bowen Fan[3,4], Ramses Ramirez[5], Hooman Mohseni[2], Michael A. Mischna[6], Michael H. Hecht[7], Liam J. Steele[3,8], Felix Sharipov[9], Edwin S. Kite[3,*]

1. Aeolis Research, Chandler, AZ.

2. Northwestern University, Evanston, IL.

3. University of Chicago, Chicago, IL.

4. Now at: Yale University, New Haven, CT.

5. University of Central Florida, Orlando, FL.

6. Jet Propulsion Laboratory, California Institute of Technology, Pasadena, CA.

7. MIT Haystack Observatory, Westford, MA.

8. Now at: European Center for Medium-Range Weather Forecasts, Reading, UK.

9. Universidade Federal do Paraná, Curitiba, Paraná, Brazil.

*Corresponding authors, mir@aeolisresearch.com and kite@uchicago.edu

Contents of this file

Supporting text.

1. Calculation of optical properties of engineered aerosols.

We calculated optical properties for two material compositions: metal particles (one type of Al rod), and carbon particles (two sizes of graphene disks).

In previous work (Ansari et al. 2024), we simulated 9 μm-long metal nanorods with an aspect ratio of 60:1 using the finite difference time domain (FDTD) method in Ansys Lumerical. In this paper, we carried out similar simulations for 8 μm-long nanorods with a width of 60 nm (133:1 aspect ratio). These particles turn out to be more than twice as mass-effective as the previous design. The FDTD method can numerically calculate an object's response to a pulse of light that contains the desired range of wavelengths. The simulated cross-section is square, but results for circular cross-sections are very similar (Fig. S3 in Ansari et al. 2024). The key output needed for input to the climate simulations are scattering and absorption cross-sections, and the scattering asymmetry (Figs. S1-S2).

Description of metal-particle models. We used the aluminum refractive-index data from Rakić (1995) as input to our nanophotonics simulations. We saved 150 output points in the wavelength range 0.24-55 μm with a mesh size of 15 nm. The climate models used here require optical properties of the particles averaged over different orientations. To account for the random orientation of the nanorods in the atmosphere of Mars, we rotated the nanorods in 5 azimuthal and 5 polar angles, resulting in a total of 25 orientations. The simulated angles were {0, 30, 45, 60, 90}°. Then, we interpolated the data of the 25 spatial orientations uniformly in angle in space (over spherical coordinates). Finally, we averaged the interpolated results over the first quadrant of the spherical coordinates to find the angle-averaged results (Table S1). A comparison of the angle averaged extinction cross-section and scattering asymmetry for aluminum 9-μm (60:1) and 8-μm nanorods (133:1) is shown in Fig. S2. The 8-μm particles have an extinction cross-section ~1/4 that of the 9-μm particles, but they are 1/8 of the volume and 1/8 of the mass. Therefore, they are ~2× more mass-effective on a per-unit extinction cross-section basis.

Description of graphene model. We used Ansys Lumerical's FDTD method for simulating graphene disks. Two designs were considered: graphene disks of 1 μm diameter (for a peak absorption at ~20 μm wavelength) and graphene disks of 0.25 μm diameter (peak absorption at 10 μm wavelength) (Fig. S3).

Graphene's optical response to light can drastically change based on the measurement substrate, but we need to know the optical properties of free-floating graphene. Hence, finding a set of optical material data that correctly captures graphene in atmosphere is quite challenging. We considered two wavelength regimes. (1) For wavelengths greater than 8 μm, a Drude model (Fermi level energy of 0.6 eV) is used to estimate the conductivity of a monolayer of graphene. The simulations in this regime use a 2D geometry (which doesn't have thickness). The mesh in these simulations is 10 nm. (2) The Drude model is not accurate at shorter wavelengths due to electronic resonance modes in graphene. For wavelengths between 0.2 μm and 8 μm, we used the experimental data of Tikuišis et al. (2023). While the graphene is on a silicon carbide substrate in these experiments, the authors attempted to minimize the interaction of graphene with the substrate in order to make the measurement quasi-free standing. Our simulations in this regime use 3D geometry. The thickness of the 3D cylinders of graphene is set to 0.3 nm to mimic the thickness of a monolayer of graphene. The *z*-direction mesh in these simulations is 0.05 nm around the graphene and 10 nm everywhere else. In all other directions the mesh is 10 nm uniformly.

In total, we ran three simulations to cover the entire wavelength spectrum. First, we use the Drude model to simulate higher wavelength data. To ensure that the simulation times are manageable, we ran two simulations at shorter wavelengths. The first simulation covers wavelengths from 0.2-0.3 μm (which is important because it sets the interaction of the graphene with biologically damaging UV radiation) and the second simulation runs from 0.3-8μm. We concatenated the data of the three simulations to collect 194 data points from 0.2 μm to 55 μm (Table S2).

Since the disks have two axes of symmetry, we rotated graphene disks in the azimuthal angle only. As the 2D geometries cannot be rotated in our simulation tool by default, we assumed a cosine dependency of the simulation output on rotation angle for all wavelengths. When the graphene disk rotates azimuthally, its geometrical cross-section changes by the

cosine of the angle. As a result, when the disk is parallel to the light's direction of propagation, the geometrical cross-section is zero. In total, we averaged over 1292 orientations to find the angle averaged outputs. Fig. S3 and Table S2 give the angle averaged extinction cross-section for 1-μm and 0.25-μm diameter disks.

Graphene disks transmit most sunlight but block UV similar to ozone. The graphene UV feature has a center position and full width at half maximum of 0.27 μm and ~0.1 μm, which is similar to that of O_3 (Hartley band at 0.255 μm) so has similar UV-protecting effects. Since $\tau_{vis} > 0.2$ (at 0.67 μm) for strong warming (Table S3), and the ratio of graphene absorption at 0.27 μm to that at 0.67 μm is >5, the graphene is optically thick ($\tau > 1$) at the center of the UV absorption feature. Thus, the amount of graphene needed for warming would define an optically thick ($\tau_{UV} > 1$) layer near the boundary between the UV-B and UV-C bands (similar to ozone), reducing the flux of biologically damaging UV at the surface.

Practicality. While graphene is a lightweight material with acceptable absorption, some practical concerns need to be answered.

The placement of the absorption peaks of graphene disks changes drastically with varying size of disks, number of layers of graphene, and graphene disks' Fermi energy level. Materials present in the environment of graphene disks can affect their doping level (and hence Fermi energy) causing drastic shifts in the wavelength of the peak of the absorption. Fang et al. (2013) have studied the effect of Fermi energy level and disk size on the graphene's response to light.

Producing a monolayer of graphene and shaping it into uniform disks requires advanced nanofabrication capability and has been heavily researched for nearly two decades (Mbayachi et al. 2021). While some methods of obtaining a monolayer of graphene are more scalable, turning graphene sheets into uniform disks of a certain size is not trivial. Using lithography and etching is a solution that can result in higher uniformity, but at the cost of throughput, making it impractical for warming Mars. Some alternative methods of growing graphene disks have been suggested (e.g., He et al. 2013). However, the throughput and uniformity of these methods might not be enough to produce the type of particles necessary for making climate change. We find that both disk sizes of 250 nm and 1000 nm can warm Mars

(Fig. S5), suggesting that a variation in size by a factor of 4 might be acceptable; however, disks resonating at 15 μm would likely not warm Mars much as CO_2 already absorbs strongly at that wavelength.

Graphene monolayers can bind via Casimir and van der Waals forces to form multilayers of graphene or graphite (Klimchitskaya & Mostepanenko 2013). This means that the graphene disks tend to agglomerate making storage in small spaces in air impossible. To alleviate the problem, the disks either need to be held in a liquid or be given enough volume that they aren't interacting. This significantly complicates the transportation and dispersion of the particles in Mars' atmosphere.

Graphene requires modification ("doping") to attain high resonance peak amplitude. Free electrons in graphene oscillate with the incoming electromagnetic field and create a resonance response in absorption at certain wavelength. As the number of free carriers increase, the resonance peak amplitude increases while the resonance wavelength becomes shorter (Neto et al. 2009). The number of free electrons available in graphene is determined by its Fermi energy. Typically, higher Fermi energies allow for more free carriers and stronger resonance responses. Graphene in its neutral form is a semimetal and does not resonate strongly with electromagnetic field. However, the carrier concentration of graphene can be easily manipulated by using other materials to dope it. Chemical doping is a method of doping graphene (Guo et al. 2011) that is attractive for this application. Graphene can be chemically doped by (1) Substitutional doping where a dopant atom replaces C atoms at some lattice sites. (2) Modulating the doping via chemical species adsorbed on the surface of the graphene (Liu et al. 2010).

However, adsorbed molecules can be desorbed by water or oxygen in the atmosphere. Method (1) is more robust although it introduces new challenges. To do substitutional doping, a dopant precursor must be made available and needs to be broken down so that the atomic form of the dopant is available. These two requirements can significantly change the energy and mass requirement of this solution. As an example, nitrogen is a popular dopant for graphene. Nitrogen is abundant (3% by volume) in Mars' atmosphere. The two main methods of chemical doping with nitrogen are in situ and ex situ (Deokar et al. 2022). In the former there is a need for particular precursors for nitrogen and these need to be present during the growth

of the graphene. The latter requires thermally annealing the graphene layer in a suitable environment.

2. How the particles are added to the climate models. The graphene disks are added to the climate model as a 16:1 (number ratio) mix of 250 nm diameter disks and 1000 nm diameter disks. The combined broadside-on area is therefore $16 \times (\pi\ 0.125^2) + (\pi\ 0.5^2) = 1.57\ \mu m^2$. The asymmetry parameter of the mixture, g_{mix}, is calculated via

$$g_{mix} = g_p\ (1 - (\ r\ (\ q_{sca} / p_{sca})\ /\ (\ r\ q_{sca} / p_{sca} + 1\ )) + g_q\ (\ r\ q_{sca} / p_{sca})\ /\ (\ r\ q_{sca} / p_{sca} + 1\ )) \qquad (1)$$

where r is the mixing ratio of q to p in particle number, q_{sca} is the scattering cross-section of particle type q, p_{sca} is the scattering cross-section of particle type p, g_q is the scattering asymmetry of particle type q, and g_p is the scattering asymmetry of particle type p.

For numerical reasons, we add the disks to the model in sets of 1700 (i.e., 1600 small disks and 100 larger disks). The particle volume flux was related to the particle optical depth using the equivalent spherical diameter. To calculate the equivalent spherical diameter for graphene, which is a 2D material, we assumed an areal density of 0.77 mg/m^2 and a three-dimensional density of 2,267 kg/m^3. This gives an equivalent spherical diameter of $2 \times ((0.77\ mg/m^2 \times 1.57\ \mu m^2 / 2{,}267\ kg/m^3) / (4\pi/3))^{1/3} = 0.101\ \mu m$ for 17 disks, and 0.467 μm for a set of 1700 disks. The equivalent spherical diameter for the Al nanorods is $2 \times ((0.06 \times 0.06 \times 8) / (4\pi/3))^{1/3} = 0.38\ \mu m$.

The column mass required for optical depth unity at the reference wavelength of 0.67 μm ($\tau_{vis} = 1$) is calculated as follows. For the graphene disk mix, the orientation-averaged extinction cross-section for a set of 17 disks is 0.0207 μm^2. The geometric broadside-on cross-section is 1.57 μm^2. (Graphene is almost transparent in the visible). The areal mass density of graphene is 0.77 mg/m^2. Therefore $\tau_{vis} = 1$ is achieved for $(1\ m^2 / 0.0207\ \mu m^2) \times (1.57\ \mu m^2 \times 0.77\ mg/m^2) = 58$ mg/m^2 column mass of graphene particles. For the 8 μm-long dimension, 60 nm-short dimension aluminum rods that are considered in this study, the orientation-averaged extinction cross-section of 1 particle is 0.493 μm^2. The mass of 1 particle is $2700\ kg/m^3 \times 8\ \mu m$

$\times$ 60 nm $\times$ 60 nm = 7.78×10^{-17} kg. Thus, the column mass at $\tau_{vis} = 1$ is $(1/0.493\ \mu m^2) \times 7.78 \times 10^{-17}$ kg = 158 mg/m^2 column mass of aluminum particles.

Particles must be designed to degrade; for example, on being brought into human habitats via airlocks, and to prevent unsustainable accumulation/build-up on the Mars surface. Surface albedo changes are not modeled in this study.

3. Calculation of the surface-warming effect of the particles using a 3D climate model.

Details of model setup: For the MarsWRF global runs to steady state that are shown in Figs. 2-4 and summarized in Table S3, we use a single model grid whose resolution is 60×36×52 latitude-longitude-height. The model top is set at 120 km (the layers are tabulated in Li et al., 2025). For the long-duration global runs, timestep is varied from 30 s to 180 s (the model uses Martian seconds, which are just under 3% longer than SI seconds). The radiative transfer uses a correlated-k scheme, referred to as the "KDM scheme," that treats both shortwave and longwave forcing (Mischna et al. 2012). The KDM scheme uses Planck-weighted averaging (215 K for the infrared bands, 6000 K for the solar bands) to down-sample the high-spectral-resolution engineered-aerosol optical properties to the 14 bins typically used in the KDM scheme (see Ansari et al. 2024 for details). In a very limited number of MarsWRF SCM simulations, we instead use 112 bins. Radiation physics calls are made every 15 Mars minutes. The surface layer scheme is a Monin-Obukhov scheme, and we use a Martian 12-layer subsurface heat diffusion scheme. The planetary boundary layer scheme is a YSU 1st order closure scheme (Hong et al., 2006), with Mars implementation similar to that in Richardson et al. (2007). The water cycle is turned off. The surface thermal inertia map, surface albedo map, obliquity, and orbital parameters are for present-day Mars.

Terrain-following modified-η coordinates are used to define the z-levels in the model (where $\eta = P\text{-}P_{top}/P_{surf}\text{-}P_{top}$, where P is local pressure, P_{surf} is surface pressure, and the fixed P_{top} is the model-top pressure).

Runs are started cold, with an equilibrated atmosphere and CO_2 cycle designed to represent modern Mars. They are run for a period exceeding 2 e-foldings of the nanorod loading, with results generally examined after 6 simulated Mars years, though most runs were extended for over a Martian decade. Run output is summarized in Table S3. Runs start at

northern spring equinox. Mars' orbit is eccentric, so the time between the northern spring equinox and northern autumn equinox is significantly longer (and less illuminated by the Sun) than the time between southern spring equinox and southern fall equinox. This is why the southern hemisphere warm season is hotter than the northern hemisphere warm season (Fig. S13). Limitations include neglect of dust-air temperature decoupling, which is significant above 40 km (Haberle et al. 2025).

The particle gravitational settling speed (terminal velocity) for rods and disks was calculated using an analytic approach appropriate for the rarefied-gas regime (Sharipov 2016). This is ~4 μm/s for graphene disks at 100 Pa (the settling speed does not depend on the disc size, provided that the size is smaller than the equivalent free path). We impose a dry deposition velocity of no less than 0.3 mm/s in the lowest model layer (~10 m thick), corresponding to non-gravitational-settling particle removal processes (such as diffusion): this is important for graphene. For the Al rods considered in this study, the settling speed at 100 Pa is 0.6 mm/s. MarsWRF internally calculates gravitational settling speed via a Cunningham slip correction formula that assumes spherical particles. Therefore, we set the gravitational settling speed by choosing a particle diameter that gives the correct (analytically calculated) particle fall speed for non-spherical particles. This is 0.073 μm for the Al rods and a negligibly small value (6 nm) for the graphene disk mix. Particle atmospheric lifetime may exceed our estimates since some particles likely get re-lofted, for example, by springtime CO_2 sublimation, rather than permanently settling at the surface. We did analytic calculations in the free-molecular limit to determine the diffusivity, D, of graphene disks and Al rods, finding (for p = 1000 Pa and T = 200 K), $D = 6.5 \times 10^{-10}$ m^2/s and 1.0×10^{-8} m^2/s, for the larger and smaller graphene disks, respectively, and $D = 5.6 \times 10^{-10}$ m^2/s for the Al rods.

Details of plume-tracking procedure: For the 'high-resolution' simulations shown in Figure 1, we use MarsWRF as a nested model with two embedded nests. The top-level domain ("d01") has 2×2° resolution (180×90 gridpoints, ~120 km/grid at the equator). We employ the same 52-layer vertical grid as the lower resolution GCM cases. Each level of nesting ("d02" and "d03"), has an increase in resolution of 3× its parent level, providing resolution as high as ~13 km/(grid cell) at the equator in "d03". As illustrated in Figs. 1a, b, the "d03" domain covers ~26.67°×26.67°.

The plume injection sites for these high-resolution runs are the same as the low resolution GCM cases. In Figure 1, only the site situated at 40°N latitude, 202°E longitude is shown. This is the "Arcadia" site in our long duration runs (Table S3). To eliminate start-up transients, "d01" is run for over a Mars year (in actuality, three full Mars years were simulated before the nests were turned on, but this is not necessary) before the nested grids are turned on. Results in Figure 1 are captured ~6 sols from the time the plume is initiated. The lower resolution GCM simulations in Figs. 2-3 employ a coarser resolution of 6×5° (lon × lat), and have no embedded nests, but are otherwise identical in implementation.

The particle mass mixing ratio is always too small to directly affect the atmospheric dynamics via particle weight (in contrast to a terrestrial pyroclastic flow).

4. Calculation of the surface-warming effect of the particles using 1D climate model.

We carried out 2 types of 1D (temperature-versus-altitude) climate modeling: using the model of Ramirez (2017), and using a 1D version of the MarsWRF code.

For the first of these models, the 1D modeling procedure closely follows that used in Ansari et al. (2024) and the following description summarizes and follows previous work. The single-column radiative-convective climate model (RCM) has 201 vertical layers, 55 infrared spectral intervals, and 38 solar spectral intervals. For present Mars (solar flux = 585 W/m^2), we assume a typical stratospheric temperature of 155 K and a surface albedo of 0.22 (e.g., Ramirez & Kasting 2017). The 1D model runs warmer (218 K) for the fiducial (no warming) case than does the 3D no-warming case (203.4 K), and the 1D-simulated temperature rises more slowly with increasing particle loading than does the 3D-simulated temperature (reasons are discussed in Ansari et al. 2024). The particles are introduced into the 1D model using the 1D average of the vertical particle mass mixing ratio from a 3D simulation, which is very close to uniform.

The RCM uses log-layers that extend from the ground to the 1×10^{-5} bar pressure level (e.g., Ramirez et al. 2017). We employ a standard moist convective adjustment (e.g., Manabe & Wetherald 1967). Should tropospheric radiative lapse rates exceed their moist adiabatic values, the model relaxes to a moist H_2O adiabat at high temperatures or to a moist CO_2 adiabat when temperatures are low enough for CO_2 to condense. The RCM implements a standard solar spectrum downscaled to model spectral resolution (Thekaekara 1973).

The atmospheric pressure is a Mars-like 650 Pa with an assumed acceleration due to gravity of 3.73 m/s^2. Although we prescribe a tropospheric relative humidity of 50%, our results are insensitive to this parameter. The baseline mean surface temperature of the resultant pure CO_2 atmosphere (without nanorods) is 218 K, which is warmer than the observed global mean surface temperature of 202 K given the 1D model's lack of clouds, dust, and topography (e.g., Haberle 2013). Nevertheless, the 1D model predicts a similar ~6K difference between the blackbody temperature and the observed one (e.g., Ramirez et al. 2014), indicating that the strength of the natural greenhouse effect is correctly reproduced.

We compute the wavenumber-dependent optical depths (τ_v) for the nanorods with the following (Ramirez & Kasting 2017, Ramirez 2017):

$$\tau_v = 3\, Q_{eff}\, PC\, \Delta z / (4\, r\, \rho) \quad (2)$$

Here, *PC* is the disk or nanorod particle content (g/m^3), Q_{eff} is the extinction cross-section, Δz is the path length, ρ is the particle density (kg/m^3), and r is the equivalent spherical radius (one-half of the diameter calculated in Supporting Text section 2). This equation is then integrated over all disk or nanorod heights and across all wavenumbers.

The particles are well-mixed throughout the atmosphere between the 650 Pa surface and the 10 Pa pressure levels, replacing the 500 Pa surface and 35-km criteria, respectively, assumed in our previous work (Ansari et al. 2024).

As before (Ansari et al. 2024), we assume that the particle content scales linearly with the local pressure. In this work, we compute new RCM mass mixing ratios that yield $\tau = 1$ at a wavelength of 0.67 microns, consistent with assumed GCM optical depth criteria. Thus, instead of keeping PC constant between models, we opt here to maintain a constant optical depth.

We implement a simple procedure to calculate particle warming. For each assumed nanorod optical depth, we find the surface temperature that yields stratospheric energy balance (i.e., the net outgoing and net incoming fluxes must balance each other) (Table S4).

In order to further isolate the differences between the 1D and 3D models, we have additionally run MarsWRF in Single Column Model (SCM) mode. This allows us to eliminate any differences due to physical process treatment (radiative transfer, boundary layer convection,

etc.) and numerical choices (grid vertical structure, tropopause fixed temperatures, etc.) and examine only the impact of 1D vs. 3D representation (which is not possible when comparing the RCM with WRF). MarsWRF SCM uses all the same physics as the MarsWRF GCM, but provides a global average treatment. It is forced with the same orbital distance variations (and hence insolation variations) over the course of the annual cycle as the GCM. As the model is much faster than the GCM, we have also experimented with increasing the spectral resolution by a factor of 8. Global average results are shown in Figure S14. These suggest that the SCM with exactly the same physics and spectral resolution as the GCM slightly underpredicts warming for the same total opacity relative to the GCM, and this discrepancy likely results from the error introduced by treating the intrinsically 3D atmosphere as a 1D spatial average. However, holding the SCM model the same except for resolution, we find a larger discrepancy due to spectral resolution, with the low spectral resolution overestimating heating, likely due to unrealistically smearing opacity into wavelength regions that are actually clearer. We note that the 8x spectral resolution WRF SCM is twice as far from the WRF GCM as it is from the RCM (i.e., the non-WRF 1D model) model. Remaining differences are the imposed 155K tropopause temperature and the permanently fixed 585 W/m^2 solar forcing. These discrepancies will be examined further in future work.

5. Order-of-magnitude estimates for production of feedstock. Within the framework of our model assumptions, warming Mars by 5 K requires a flux of 5 L/s of Al particles or 2 L/s of graphene disks (Fig. S9). We provide order-of-magnitude estimates of the inputs required.

a. Graphene. The chemical energy required to produce graphene from atmospheric CO_2 (ΔH for the reaction $CO_2 \rightarrow C + O_2$) is 393 kJ/mol. From the perspective of production of O_2, an essential resource on Mars, this reaction represents a lower energy investment per O_2 molecule than the $2CO_2 \rightarrow 2CO + O_2$ process (ΔH = 566 kJ/mol) demonstrated by the Mars OXygen In-situ resource utilization Experiment (MOXIE) on Perseverance (Hoffman et al. 2022). This is because it recovers some of the energy invested in forming CO. The more energetically favorable reaction has not been considered as a candidate for oxygen production because of the substantial challenge of managing the solid carbon product compared to the relatively simple disposal of CO.

Nonetheless, co-production of graphene and O_2 theoretically has the potential to require less overall energy than producing O_2 alone. Since a large mass of O_2 is needed for propellant for launches from Mars, and humans need ~0.6 tonnes/(Mars year)/person of O_2 to breathe, it is of interest to quantify the synergy by coupling graphene and O_2 production.

Production of graphene from atmospheric CO_2 might be accomplished in two steps: Step 1, like MOXIE, uses solid oxide electrolysis (SOE) to produce O_2 and CO by the reaction $2CO_2 \rightarrow 2CO + O_2$. Step 2 converts the CO directly into graphene in a thermally coupled reactor utilizing the exothermic Boudouard reaction $2CO \rightarrow C + CO_2$. The latter step has been demonstrated on a laboratory scale (Grebenko et al. 2022) using chemical vapor deposition (CVD), a technique that lends itself to scale-up and has already been used extensively to produce carbon nanotubes. The power generated by the Step 2 reaction is most readily captured by recycling the hot, pressurized CO_2 into the Step 1 SOE system. Note that production of other forms of carbon (e.g., graphite) as an intermediate step to forming graphene could employ the same reaction. Graphene could alternatively be produced from C via methods like liquid-phase shear exfoliation (Paton et al. 2014) or flash Joule heating (Luong et al. 2020).

At a carbon density of ρ = 2,267 kg/m^3, target production of 2 L/s graphene corresponds to 382 mol/s carbon (= O_2), so 380 ktonnes of O_2 /yr. The scale-up of MOXIE is relatively straightforward (Rapp & Hinterman 2023), and it has been estimated that a reference unit producing 838 kmol/yr (3 kg/hr O_2) will mass ~1 tonne (Hintermann et al. 2022). The O_2 liquefaction hardware would mass another ~1.3 tonnes, for a total of ~2.3 tonnes not including liquefied O_2 tanks (part of the system design for launch vehicles and habitats) (Hintermann et al. 2022). Since the gas collection system and other subsystems are common to both SOE and the Boudouard reactor, the latter is likely not to add more than the mass of the SOE itself, or ~0.5 tonne. Power usage for the 838 kmol/yr system is ~25 kW, including liquefaction. The corresponding power system mass depends on what method is used to generate power. A conservative estimate is 6 tonnes (Hintermann et al. 2022), scaling from actual flown-to-Mars solar power gives 1.5 tons (Romero-Guzman et al. 2023), and more optimistic estimates are <1 tonne (e.g., Wollman & Zika 2006). Further scaling the 838 kmol/yr reference system to a system that will produce 2 L/s graphene would thus require ~360 MW. One way to think about

scale-up and deployment of a net 2 L/s carbon production is as a network of modular stations each capable of producing appropriate amounts of O_2 and power to serve as an exploration basecamp, producing graphene as a secondary product of the O_2 generation. Such an arrangement provides flexibility for meeting diverse scientific objectives. As an example, each of 100 distinct sites might be emplaced as exploration infrastructure, with each providing a minimum of 3.6 MW while generating 3.8 ktonne O_2 per year. That capability could support, for example, 3 spacecraft launches and an average population of 7,300. The corresponding landed mass per site for the carbon and O_2 production is estimated to be ~1253 tonnes for the conservative estimate of power system mass, and ~555 tonnes for the more optimistic estimate of power system mass. Depending on the usage scenario, either additional power would be provided for human life support or else O_2 could be stockpiled in tanks and production suspended while the existing power system supported a limited duration mission.

Where measured, organic carbon is only present at low concentration (0.5 kg/m^3) in Mars soil (Stern et al. 2022), so we assume graphite is made from Mars air by electrolysis rather than being obtained from soil.

In contrast to CO_2 electrolysis, scaling for graphite-to-graphene conversion at the large scales needed to warm Mars is unexplored in a spaceflight context. Scale-up is required to reach the 400 metric ton/day level because the largest graphene producer in the world currently has only 13 metric ton/day capacity (NanoXplore). However, graphene production capacity is increasing rapidly.

b. Aluminum particles. We assume 257 MJ/kg to extract Al from soil via molten regolith electrolysis, by analogy with the energy requirement to extract Al from electrolysis on Earth (Table 8 in Staley & Haupin 2000). This first (feedstock) step is likely to be the primary energy sink in the process of producing Al particles. The mining rate of regolith for a subscale (10%) test is ~7 m^3/hour at each of 100 sites, assuming 10 wt% Al_2O_3 in regolith. Conversion of planetary regolith to metals has been extensively studied in a lunar context (Williams et al. 1979). The major element composition of Mars soil is that of tholeiitic basalt, similar to that of the lunar maria but with more Cl and S. Mg is potentially promising but has not yet been explored.

Supporting References.

Bertrand, T., Kahre, M.A., Urata, R., Määttänen, A., Montmessin, F., Wilson, R.J., and Wolff, M.J., 2022. Impact of the coagulation of dust particles on Mars during the 2018 global dust storm. *Icarus*, 388, p.115239. https://doi.org/10.1016/j.icarus.2022.115239

Deokar, G., Jin, J., Schwingenschlögl, U., Kanoun, M.B., and Costa, P.M.F.J., 2022. Chemical vapor deposition-grown nitrogen-doped graphene's synthesis, characterization and applications. *npj 2D Mater Appl*, 6, p.14. https://doi.org/10.1038/s41699-022-00287-8

Grebenko, A.K., Krasnikov, D.V., Bubis, A.V., Stolyarov, V.S., Vyalikh, D.V., Makarova, A.A., Fedorov, A., Aitkulova, A., Alekseeva, A.A., Gilshtein, E., and Bedran, Z., 2022. High-quality graphene using Boudouard reaction. *Advanced Science*, 9(12), p.2200217. https://doi.org/10.1002/advs.202200217

Guo, B., Fang, L., Zhang, B., and Gong, J.R., 2011. Graphene doping: a review. *Insciences J.*, 1(2), pp.80-89. https://doi.org/10.5640/insc.010280

Haberle, R.M., 2013. Estimating the power of Mars' greenhouse effect. *Icarus*, 223(1), pp.619-620. https://doi.org/10.1016/j.icarus.2012.12.022

Haberle, R.M., Clancy, R.T., Forget, F., Smith, M.D., and Zurek, R.W. eds., 2017. *The Atmosphere and Climate of Mars*. Cambridge University Press.

Haberle, R.M., Kahre, M.A., Bertrand, T., and Wolff, M.J., 2025. Modeling studies of dust/gas non-thermal equilibrium in the Martian atmosphere. *Icarus*, 429, p.116452. https://doi.org/10.1016/j.icarus.2024.116452

Hartwick, V.L., Haberle, R.M., Kahre, M.A., and Wilson, R.J., 2022. The dust cycle on Mars at different orbital distances from the Sun: An investigation of the impact of radiatively active dust on land planet climate. *Astrophysical Journal*, 941(1), p.54. https://doi.org/10.3847/1538-4357/ac9481

Hartwick, V.L., Toon, O.B., Lundquist, J.K., Pierpaoli, O.A., and Kahre, M.A., 2023. Assessment of wind energy resource potential for future human missions to Mars. *Nature Astronomy*, 7(3), pp.298-308. https://doi.org/10.1038/s41550-022-01851-4

He, C., Jiang, S., and Shen, P., 2013. Large-scale and rapid synthesis of disk-shaped and nano-sized graphene. *Scientific Reports*, 3, p.2144. https://doi.org/10.1038/srep02144

Hinterman, E.D., 2022. Multi-objective system optimization of a Mars atmospheric ISRU plant (Doctoral dissertation, Massachusetts Institute of Technology), https://hdl.handle.net/1721.1/145095

Hoffman, J.A., Hecht, M.H., Rapp, D., Hartvigsen, J.J., SooHoo, J.G., Aboobaker, A.M., McClean, J.B., Liu, A.M., Hinterman, E.D., Nasr, M., and Hariharan, S., 2022. Mars Oxygen ISRU Experiment (MOXIE)—preparing for human Mars exploration. *Science Advances*, 8(35), p.eabp8636. https://doi.org/10.1126/sciadv.abp8636

Hong, S. Y., Noh, Y., and Dudhia, J. (2006). A new vertical diffusion package with an explicit treatment of entrainment processes. *Monthly Weather Review*, 134(9), 2318-2341. https://doi.org/10.1175/MWR3199.1

Klimchitskaya, G.L., and Mostepanenko, V.M., 2013. Van der Waals and Casimir interactions between two graphene sheets. *Physical Review B---Condensed Matter and Materials Physics*, 87(7), p.075439. https://doi.org/10.1103/PhysRevB.87.075439

Li, L., Zhao, C., Newman, C. E., Zhao, Y., Feng, J., Li, T., et al. (2025). Impacts of dry deposition processes with resolved dust particle sizes on simulating the Martian dust. *Journal of Geophysical Research: Planets*, 130, e2024JE008616. https://doi.org/10.1029/2024JE008616

Liu, H., Liu, Y., and Zhu, D., 2010. Chemical doping of graphene. *J. Mater. Chem.*, 20, pp.10928-10934.

Luong, D.X., Bets, K.V., Algozeeb, W.A., Stanford, M.G., Kittrell, C., Chen, W., Salvatierra, R.V., Ren, M., McHugh, E.A., Advincula, P.A., and Wang, Z., 2020. Gram-scale bottom-up flash graphene synthesis. *Nature*, 577(7792), pp.647-651. https://doi.org/10.1038/s41586-020-1938-0

Madeleine, J.B., Head, J.W., Forget, F., Navarro, T., Millour, E., Spiga, A., Colaïtis, A., Määttänen, A., Montmessin, F., and Dickson, J.L., 2014. Recent ice ages on Mars: The role of radiatively active clouds and cloud microphysics. *Geophys. Res. Lett.*, 41(14), pp.4873-4879. https://doi.org/10.1002/2014GL059861

437 Manabe, S., and Wetherald, R.T., 1967. Thermal equilibrium of the atmosphere with a given
438 distribution of relative humidity. *J. Atmos. Sci.*, 24, pp.241-259. https://doi.org/10.1175/1520-
439 0469(1967)024<0241:TEOTAW>2.0.CO;2

440 Mbayachi, V.B., Ndayiragije, E., Sammani, T., Taj, S., Mbuta, E.R., and Khan, A.U., 2021. Graphene
441 synthesis, characterization and its applications: A review. *Results in Chemistry*, 3, p.100163.
442 https://doi.org/10.1016/j.rechem.2021.100163

443 McClellan, J., Keith, D.W., and Apt, J., 2012. Cost analysis of stratospheric albedo modification
444 delivery systems. *Environ. Res. Lett.*, 7(3), p.034019. https://doi.org/10.1088/1748-
445 9326/7/3/034019

446 Mischna, M.A., Lee, C., and Richardson, M., 2012. Development of a fast, accurate radiative
447 transfer model for the Martian atmosphere, past and present. *J. Geophys. Res.: Planets*, 117(E10).
448 https://doi.org/10.1029/2012JE004110

449 Neto, A.H., Guinea, F., Peres, N.M.R., Novoselov, K.S., and Geim, A.K., 2009. The electronic
450 properties of graphene. *Rev. Mod. Phys.*, 81, pp.109-162.
451 https://doi.org/10.1103/RevModPhys.81.109

452 Paton, K.R., Varrla, E., Backes, C., Smith, R.J., Khan, U., O'Neill, A., Boland, C., Lotya, M., Istrate,
453 O.M., King, P., and Higgins, T., 2014. Scalable production of large quantities of defect-free few-
454 layer graphene by shear exfoliation in liquids. *Nature Materials*, 13(6), pp.624-630.
455 https://doi.org/10.1038/nmat3944

456 Rakić, A.D., 1995. Algorithm for the determination of intrinsic optical constants of metal films:
457 Application to aluminum. *Applied Optics*, 34, pp.4755-4767.
458 https://doi.org/10.1364/AO.34.004755

459 Ramirez, R.M., and Kasting, J.F., 2017. Could cirrus clouds have warmed early Mars? *Icarus*, 281,
460 pp.248-261. https://doi.org/10.1016/j.icarus.2016.08.016

461 Ramirez, R.M., Kopparapu, R., Zugger, M.E., Robinson, T.D., Freedman, R., and Kasting, J.F., 2014.
462 Warming early Mars with CO2 and H2. *Nat. Geosci.*, 7, pp.59-
463 63. https://doi.org/10.1038/ngeo2000

Rapp, D., and Hinterman, E., 2023. Adapting a Mars ISRU System to the Changing Mars Environment. *Space: Science & Technology*, 3, p.0041. https://doi.org/10.34133/space.0041

Sharipov, F., *Rarefied Gas Dynamics: Fundamentals for Research and Practice* (Wiley-VCH, Berlin, 2016).

Romero-Guzman, C., Perez-Grande, I. and Rodriguez-Manfredi, J.A., 2023. Thermal model of InSight solar panels in Martian conditions. *Acta Astronautica*, *202*, pp.476-484.

Staley, J.T., and Haupin, W., 2000, Aluminum and aluminum alloys, in *Kirk-Othmer Encyclopedia of Chemical Technology*, 4th Edition, volume 2, Kirk-Othmer.

Streeter, P.M., Lewis, S.R., Patel, M.R., Holmes, J.A., and Kass, D.M., 2020, Surface warming during the 2018/Mars year 34 global dust storm. *Geophys. Res. Lett.* 47, e2019GL083936. https://doi.org/10.1029/2019GL083936

Thekaekara, M.P., 1973. Solar energy outside the Earth's atmosphere. *Solar Energy*, 14, pp.109-127. https://doi.org/10.1016/0038-092X(73)90028-5

Tikuišis, K.K., Dubroka, A., Uhlířová, K., Speck, F., Seyller, T., Losurdo, M., Orlita, M., and Veis, M., 2023. Dielectric function of epitaxial quasi-freestanding monolayer graphene on Si-face 6H-SiC in a broad spectral range. *Phys. Rev. Materials*, 7, p.044201. https://doi.org/10.1103/PhysRevMaterials.7.044201

Williams, R.J., McKay, D.S., Giles, D., and Bunch, T.E., 1979. Mining and beneficiation of lunar ores. *Space Resources and Space Settlements* (NASA SP-428), pp.275-188.

Wollman, M.J., and Zika, M.J. Prometheus Project Reactor Module Final Report, For Naval Reactors Information, Apr. 2006. https://doi.org/10.2172/884680

485 **Supporting Figures.**

486

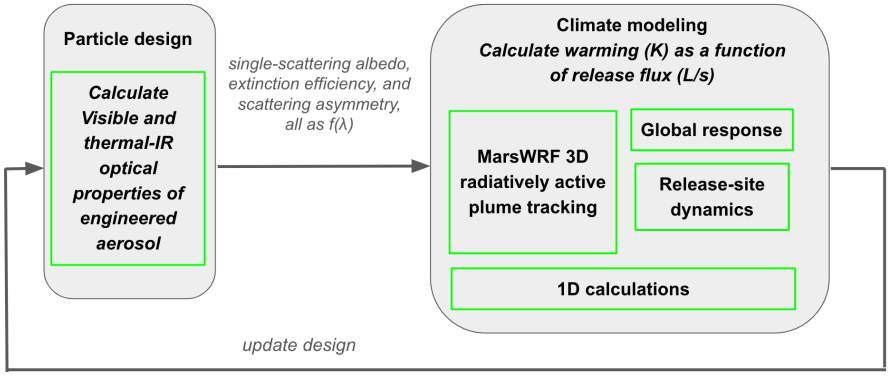

Fig. S1. Schematic of workflow.

487

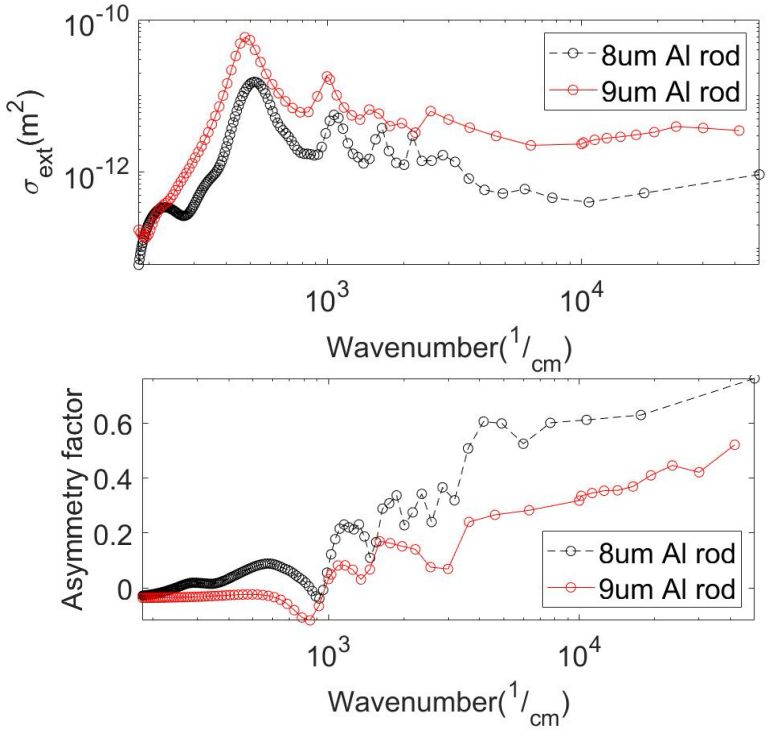

Fig. S2. Comparison of the angle-averaged scattering asymmetry and extinction cross-section in two Al nanorods. Shown are the 9-μm (60:1 aspect ratio) design from Ansari et al. (2024) (in red), and the 8-μm (133:1 aspect ratio) design from this paper (in black).

488

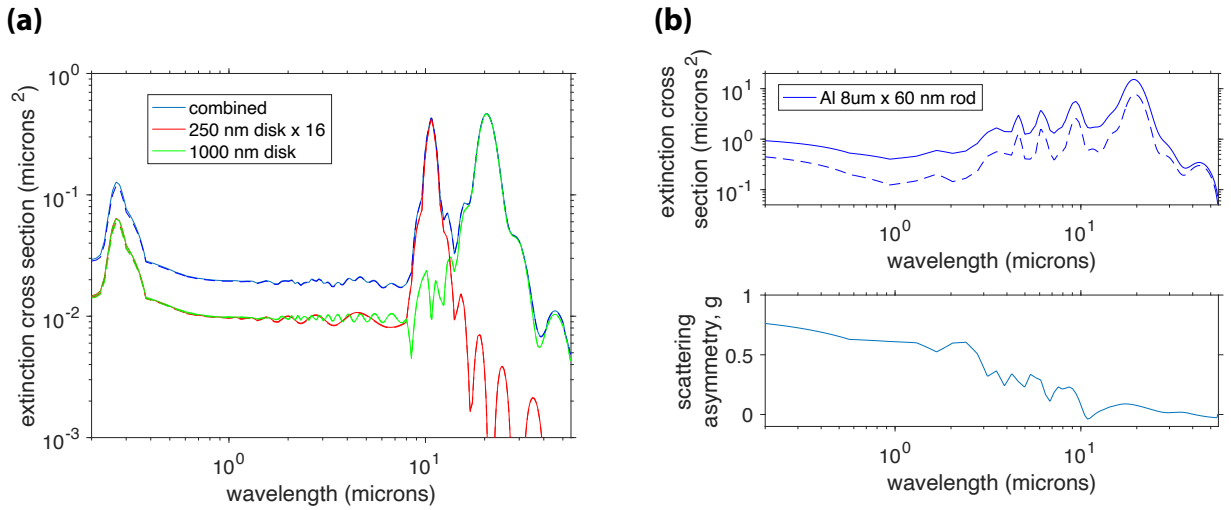

Fig. S3. Spectra for engineered aerosol (0.2-55 μm). **(a)** Graphene disk extinction spectrum. Sizes are disk diameters. Dashed lines show the absorption contribution (close to 100% except in the UV). Scattering asymmetry is close to zero. The 250-nm disk is shown multiplied by 16 for ease of comparison, and because a 16:1 number ratio of 250-nm disks to 1000-nm disks is used in most of the graphene simulations. **(b)** 8 μm, 60 nm diameter Al rod extinction spectrum. Dashed line shows the absorption contribution. Lower panel: scattering asymmetry.

489

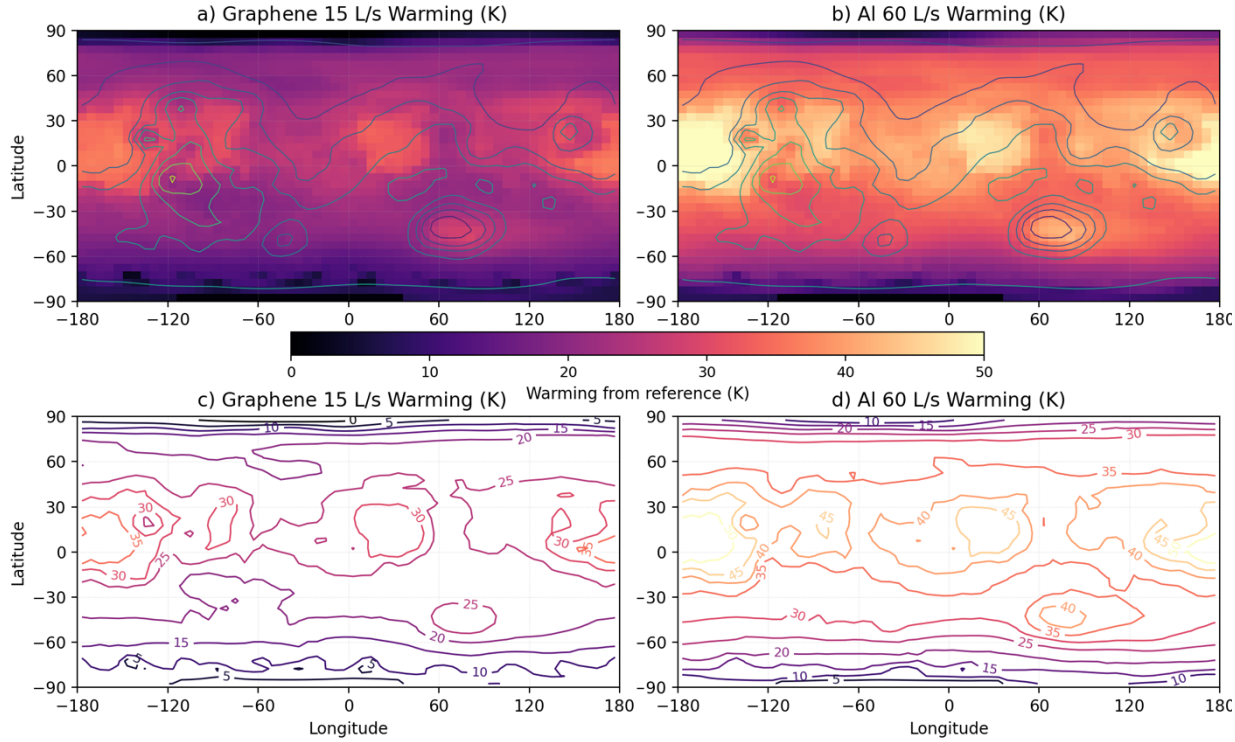

Fig. S4. Spatial structure of the annual-average warming relative to control case. (a,c) 15 L/s graphene mix (*run Cc41*). **(b,d)** 60 L/s Al particles (*run Cc16*).

490

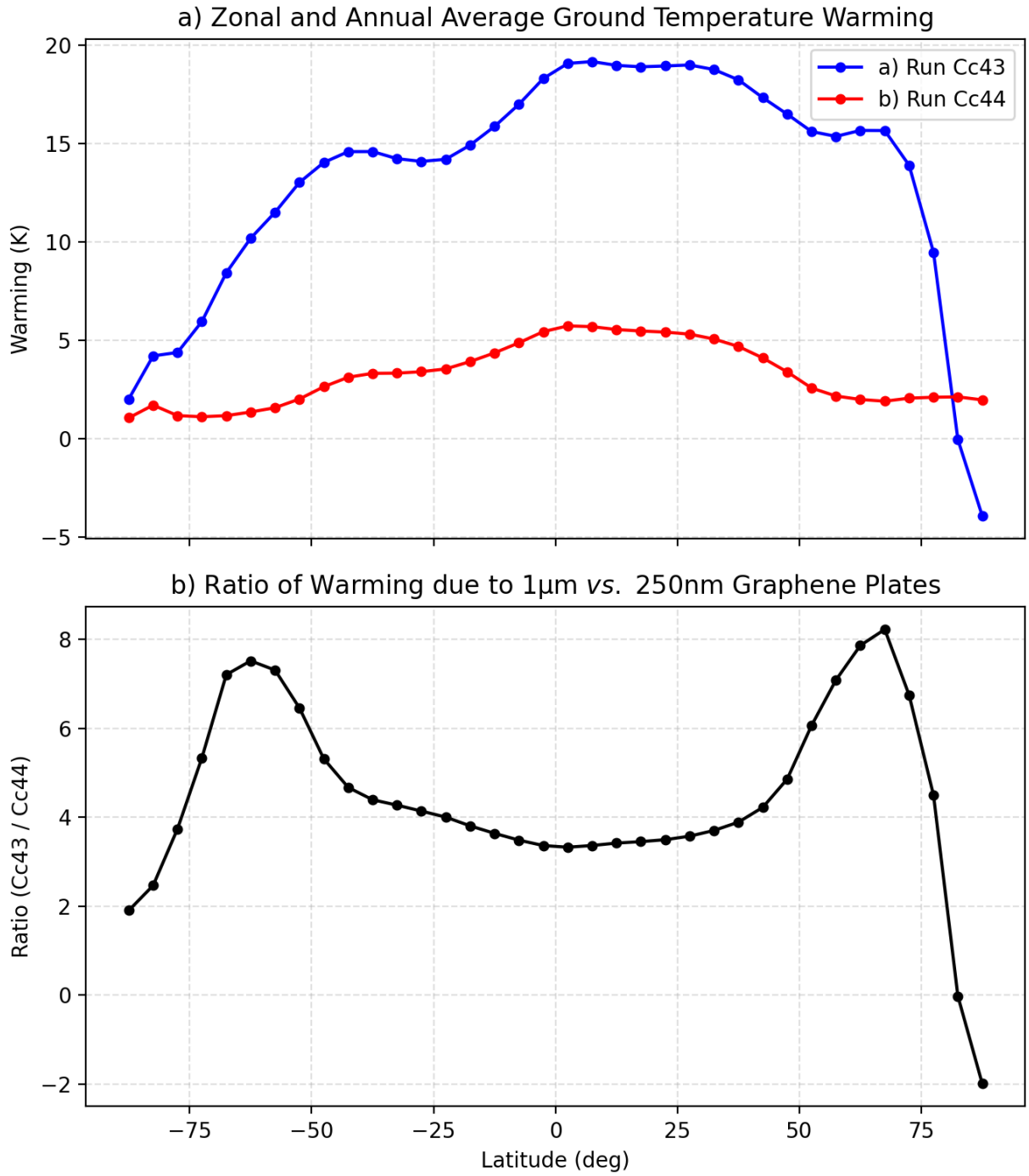

Fig. S5. Latitudinal tuning of Mars warming. a) Blue curve shows annual-average warming due to 1 μm diameter graphene disks (black) (*run Cc43*). Red curve shows warming due to 250 nm diameter graphene disks (*run Cc44*). Each curve is generated from the true diurnal average ground temperature calculated on-the-fly from every dynamical timestep (typically 180 s at this resolution) by the GCM. These output quantities are then zonally and annually averaged, and then differenced from the same output generated for the reference (no nanoparticle) case (*run Cc8r*). **b)** The ratio of *Cc43* to *Cc44* warming shows that at the equator,

the 1-μm disks provide just over 3.5x more warming than the 250-nm disks. However, the ratio varies with latitude. Both disk types lose their warming effectiveness at the poles, which remain very cold. At the north pole, the 1-μm disks actually generate net cooling.

491

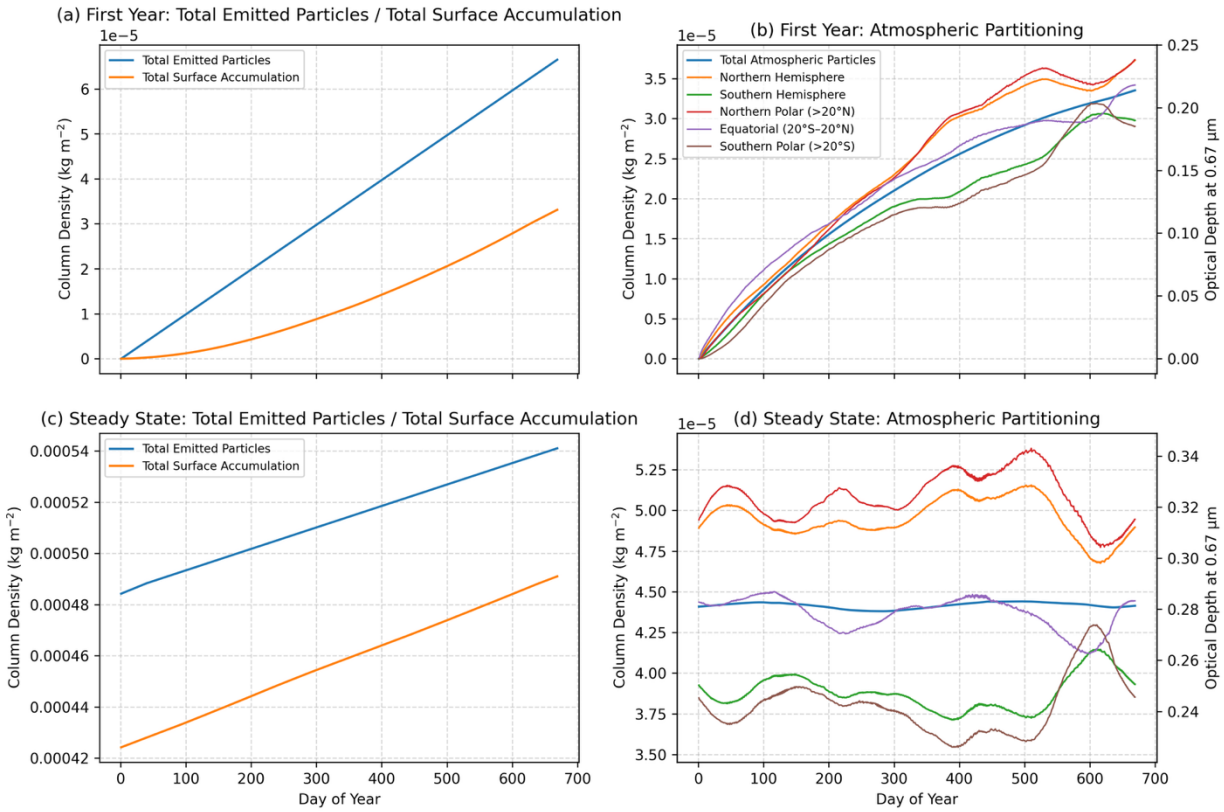

Fig. S6. Seasonal variation of nanoparticle emission, settling, and atmospheric column density and τ_{vis}. (a,b) during build-up. **(c,d)** in steady state. For (a,c), blue is emitted particle mass, orange is surface accumulation (both kg/m^2). For (b,d) blue = global average, represented as column density on left axis (kg/m^2) and 0.67 μm optical depth on right hand axis. The portioning between northern hemisphere (orange) and southern hemisphere (green) is indicated. This global abundance can also be separated into three equal area regions including the equatorial belt (purple), northern "polar" (latitude poleward of 19.47°N, in red), and southern polar (poleward of 19.47°S, in magenta). The x-axis labels the day number of a single Mars year, with day 0 at the northern spring equinox (L_s=0°). All output from *run Cc16.*

492

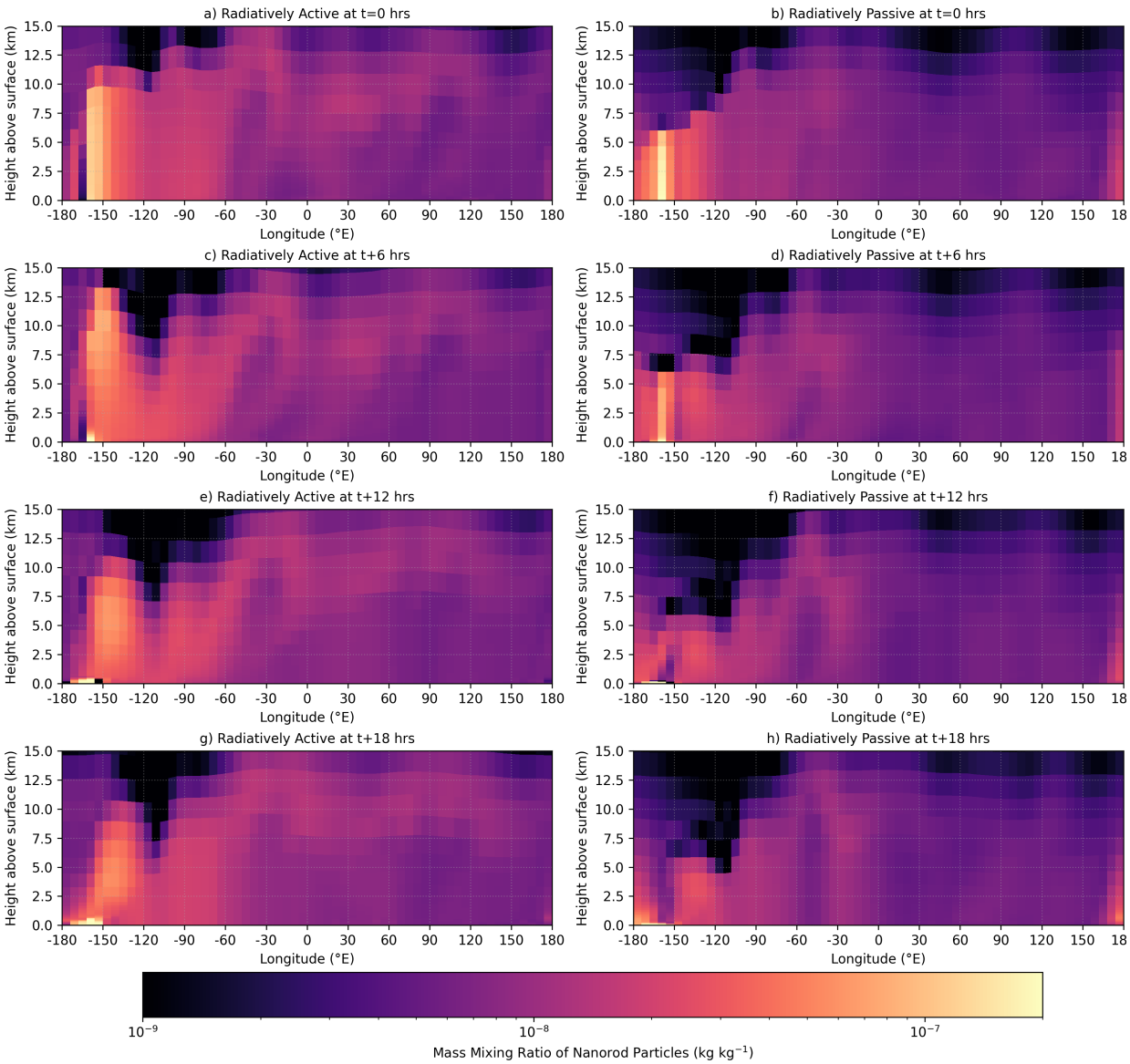

Fig. S7. Radiative feedback leading to self-lofting and aiding plume deployment. Longitude-height cross-section through the deployment plume with **(a,c,e,g)** and without **(b,d,f,h)** radiatively active feedback. Shaded quantity is the nanorod mass mixing ratio (dimensionless). (a,c,e,g) 12.5 L/s graphene, ~30 sols into deployment (*run Cc11*). (b,d,f,h) Injected the same 12.5 L/s of graphene but with radiative feedback disabled, ~30 sols into deployment (*run Cc8*). For both simulations, 4 timesteps are shown, 6 Martian hours apart.

493

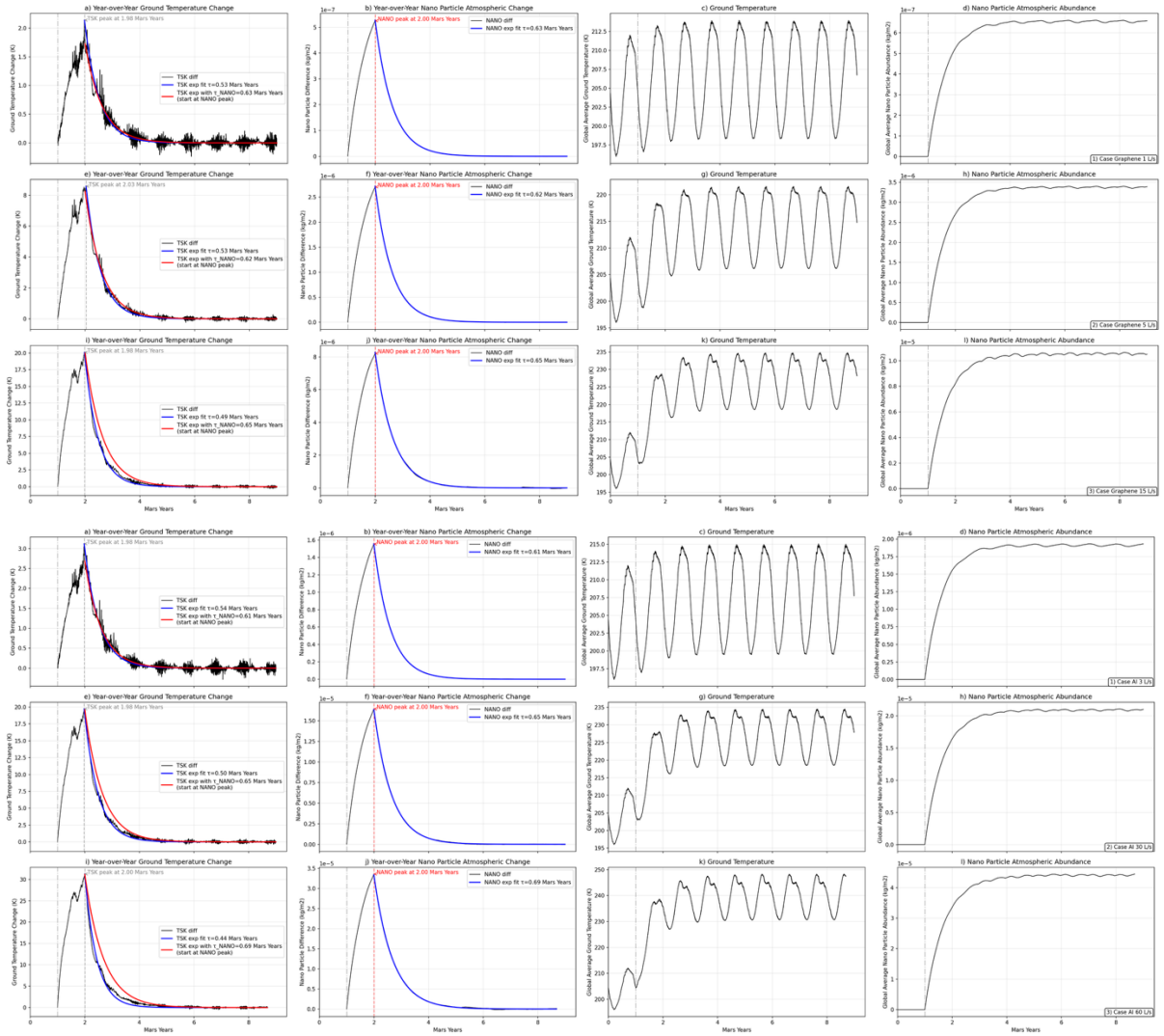

Fig. S8. Atmospheric nanoparticle increase and ground warming: Initial year increase followed by exponential decline as Mars' atmosphere approaches steady-state warming. First column: warming relative to the same timestep from the previous year, at each timestep after spin-up (first year excluded as it is in steady state). This algorithm removes the seasonal cycle in temperature. The x-axis units are Mars years. Blue line: fitting the evolution to an exponential decay. ΔT: annual warming. τ: warming timescale. Second column: Year-over-year trends for nanorod abundance (given as average column density). Third column: ground temperature trend. Fourth column: Nanorod abundance trend. All runs shown are for the equatorial release site. Each run is labelled in the lower right corner of the right-most panel.

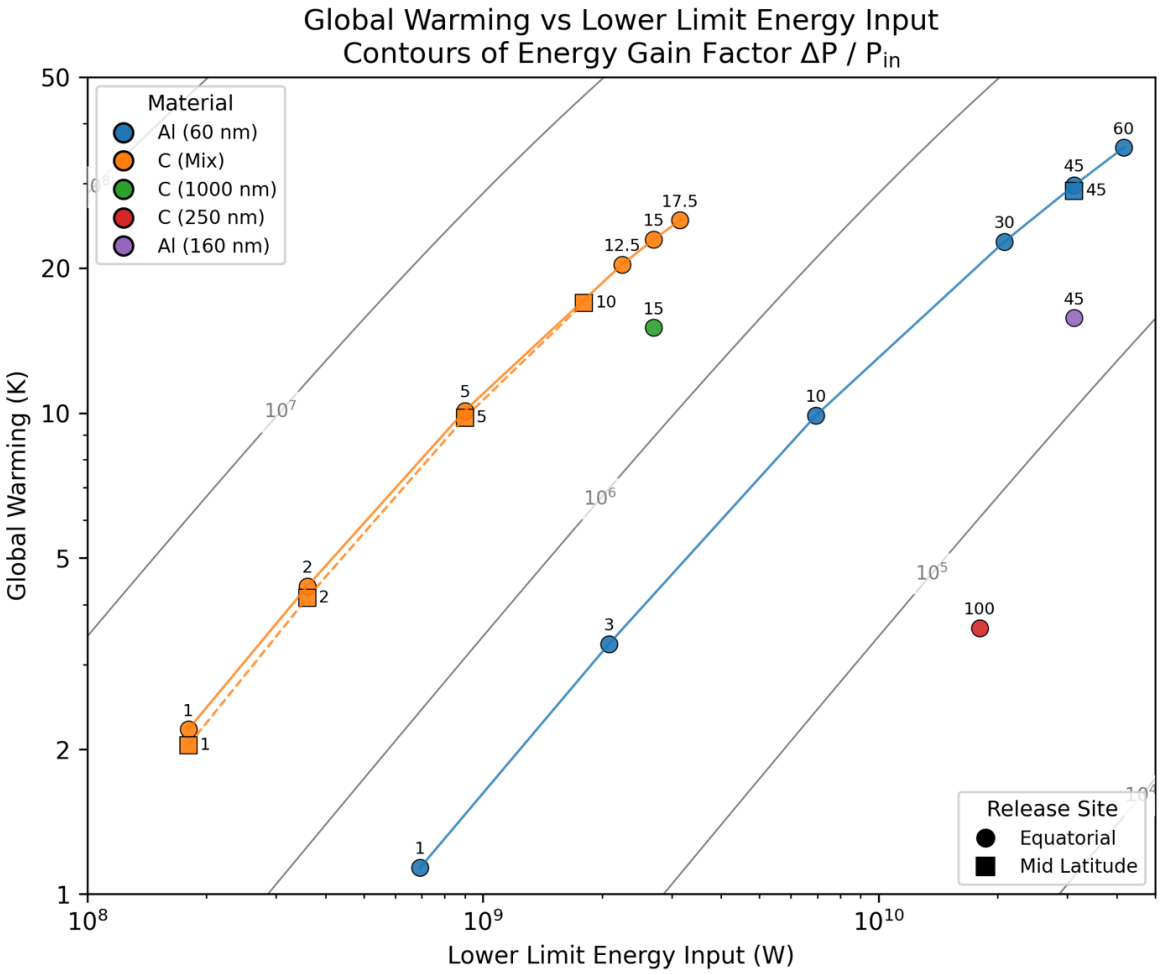

Fig. S9. Steady-state temperature response as a function of the steady-state energy input. Data points are from the dynamic plume tracking GCM. The x-axis is the power needed to create the feedstock needed for the specified rate of nanoparticles for injection (see text). Output are shown for all model cases from Table S3 and are as labeled on the plot. The marker numbers correspond to injection rates in L/s. The continuous thin contours show the "energy gain factor", which is calculated as the extra power from the increased ground temperature (the blackbody emission from the new ground temperature - σT_{av}^4 - minus the black body emission from the reference case ground temperature) divided by the amount of power needed to make the nanoparticles. The labels on the thin black contours correspond to the numerical value of this gain factor for a given warming and energy input rate. Solid blue line and solid orange lines correspond to release at Elysium. Dashed orange line corresponds to release at Arcadia. The red symbol (*run Cc49*) shows the Al particle design emphasized in previous work (Ansari et al. 2024); the graphene disk mix is ~20× more energy-effective (See Table S3 for detail). Energy input assumes 180 MW/L for graphene disk production and 693.9 MW/L for Al rod production (see text).

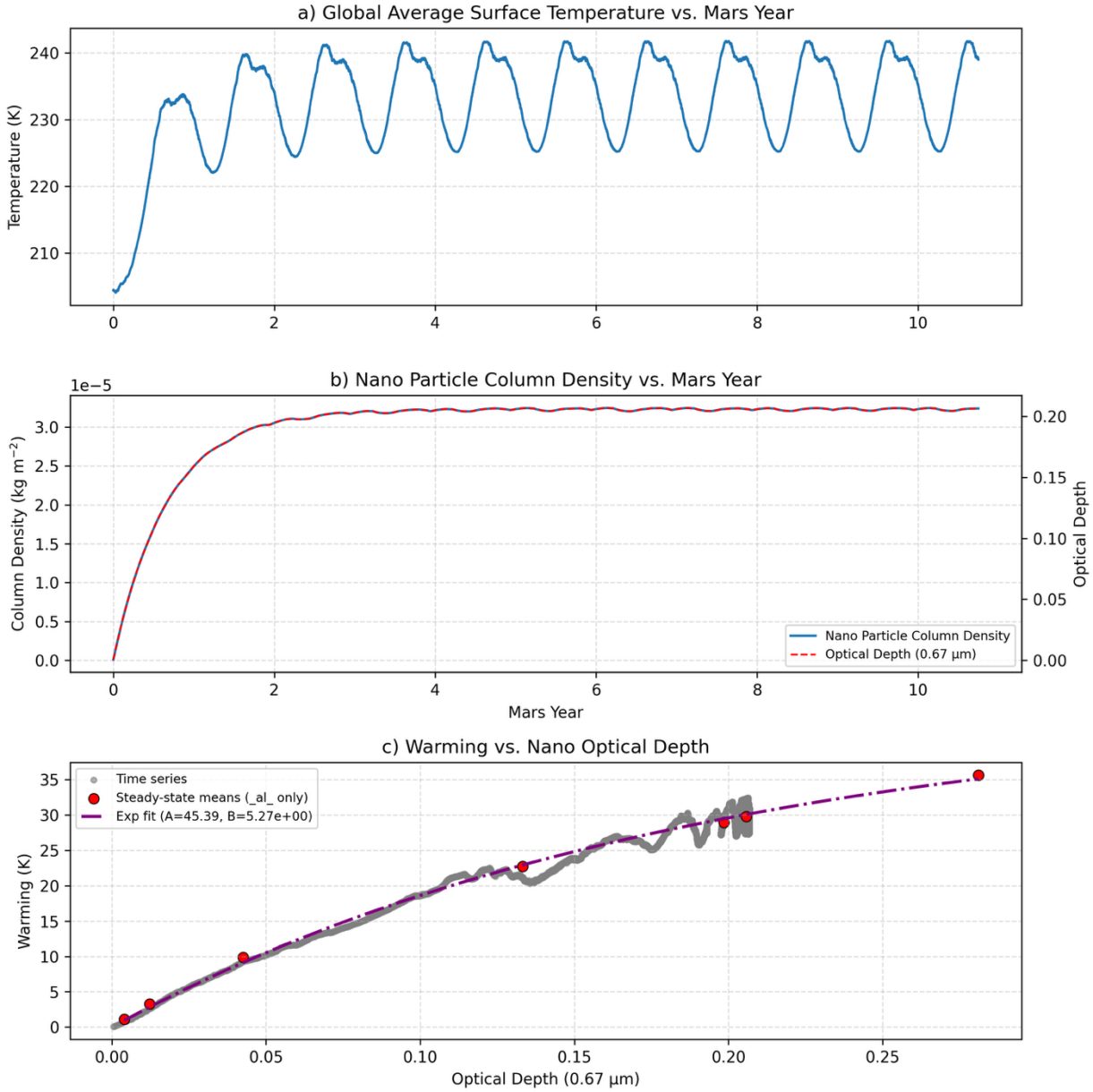

Fig. S10. Transient and Steady State Temperature Response. (a) Transient temperature response for 45 L/s Al rod loading (*run Cc17*). The global average for every sol is plotted. (b) Time history of global average nano particle column density and visible (0.67 μm) optical depth. (c) Relationship between surface temperature warming and visible optical depth (τ_{vis}) during transient warming. Gray line shows the continuous trajectory during the simulation from (a) and (b). Warming is calculated by taking the instantaneous global average T_{surf} and subtracting from it the global average T_{surf} for that sol-of-year from the unperturbed case. Red dots show the steady state annual average warming and nano rod visible opacity from the Al cases listed in Table S3. The fit to the steady state values is the warming, $\Delta T=A(1-e^{-B\tau})$. Note

the fit is likely only valid to moderate optical depths where significant sunlight still penetrates to the surface.

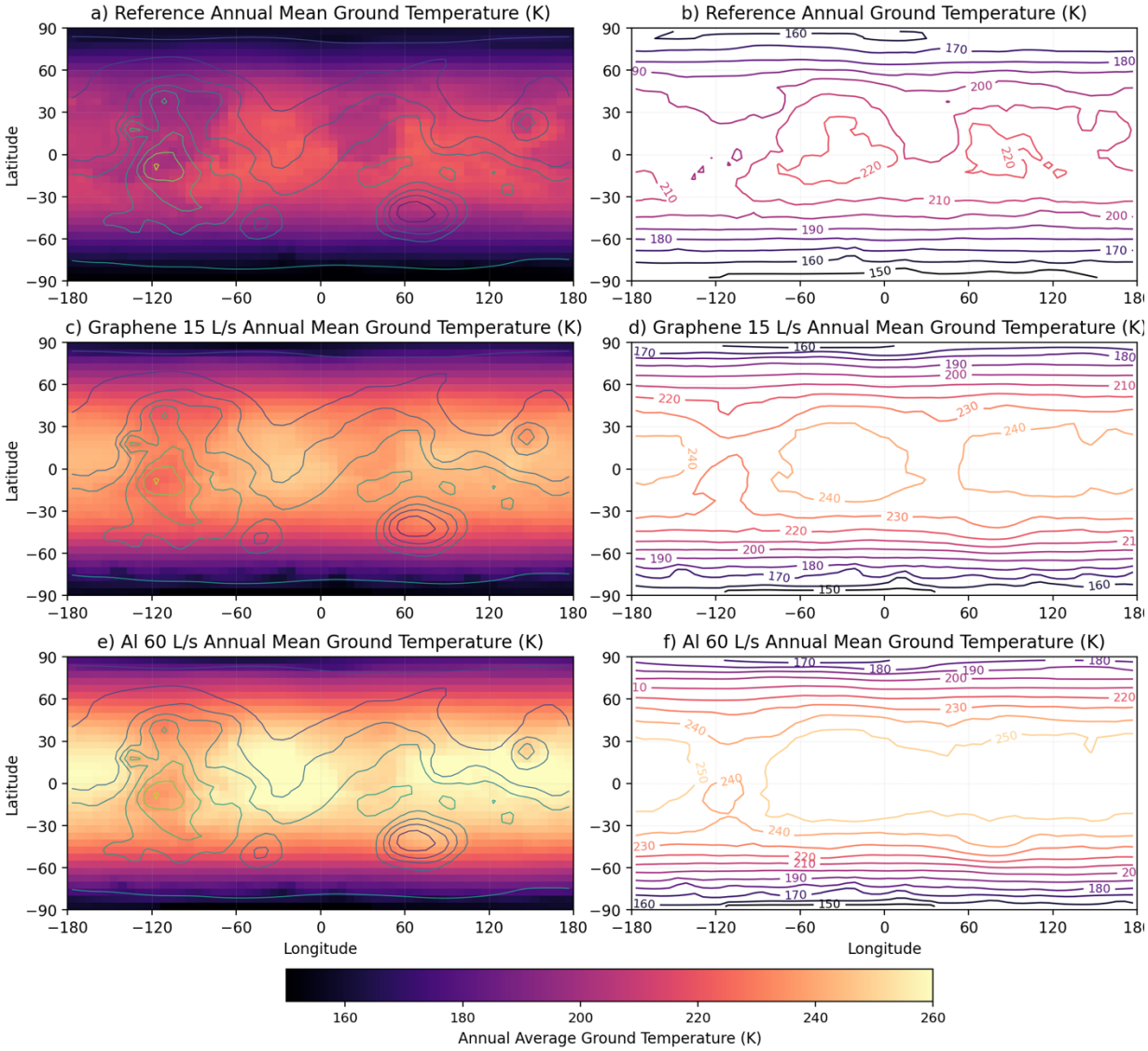

Fig. S11. Global average temperatures (K) in steady state. (a,b) Control case (no warming). (c,d) Graphene 15 L/s (*run Cc41*). **(e,f)** Al rods 60 L/s (*run Cc16*).

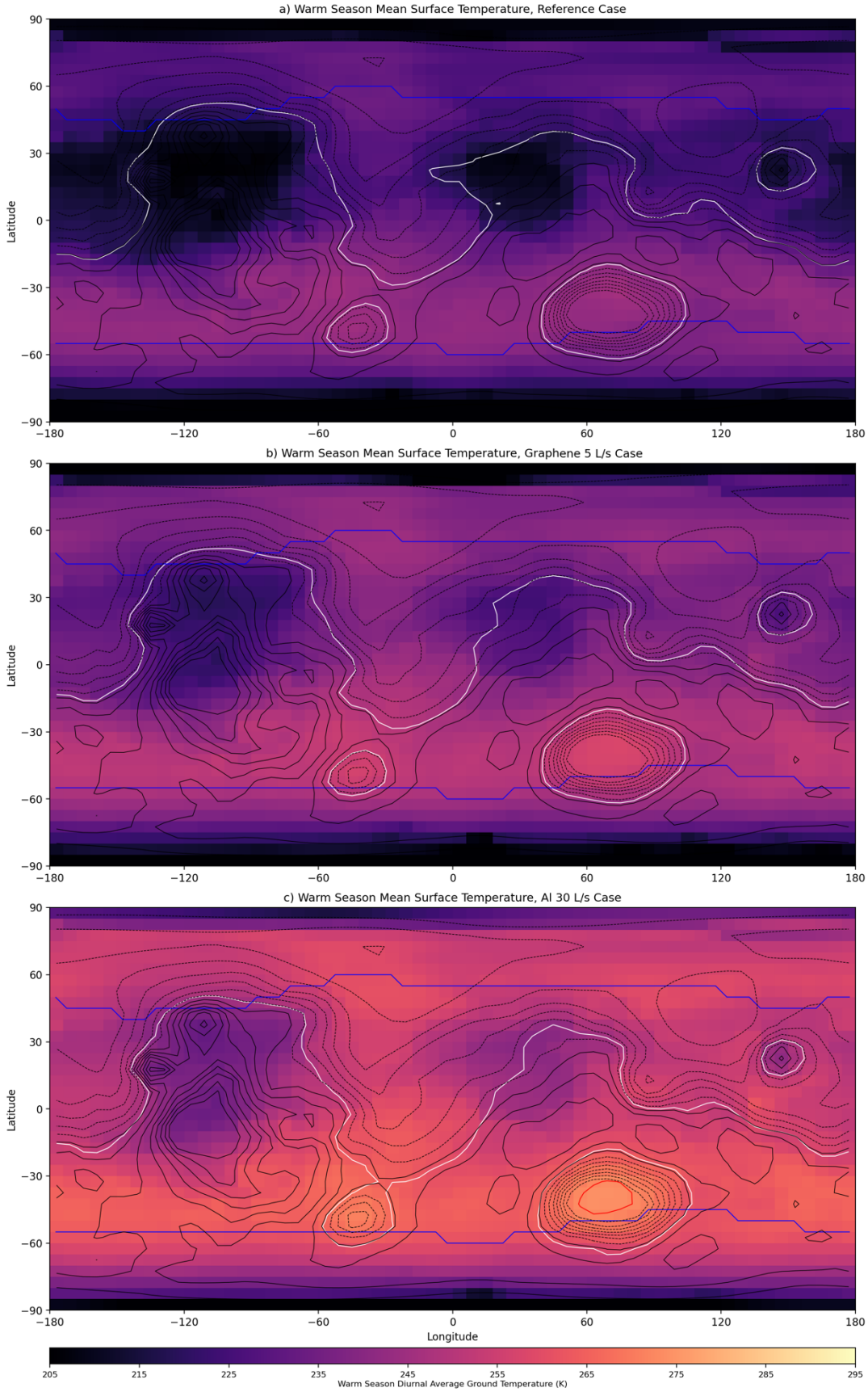
a) Warm Season Mean Surface Temperature, Reference Case
b) Warm Season Mean Surface Temperature, Graphene 5 L/s Case
c) Warm Season Mean Surface Temperature, Al 30 L/s Case
Latitude
Longitude
90
60
30
0
−30
−60
−90
−180
−120
−60
0
60
120
180
205
215
225
235
245
255
265
275
285
295
Warm Season Diurnal Average Ground Temperature (K)

Fig. S12.

Warm-season average temperatures for control case, and sensitivity test for lower flux. **(a)** Control case (no warming) (*run Cc8*). **(b)** Graphene disks, 5 L/s (*run Cc34*). **(c)** Al particles, 30 L/s (*run Cc29*). White contour corresponds to 610 Pa (~6 mbar) mean pressure level. Blue lines: Approximate latitudinal (equatorward) extent of ice at <1 m depths. Topographic contours correspond to elevations of −5 and −2 km (dashed), and 0, +2, and +5 km (solid).

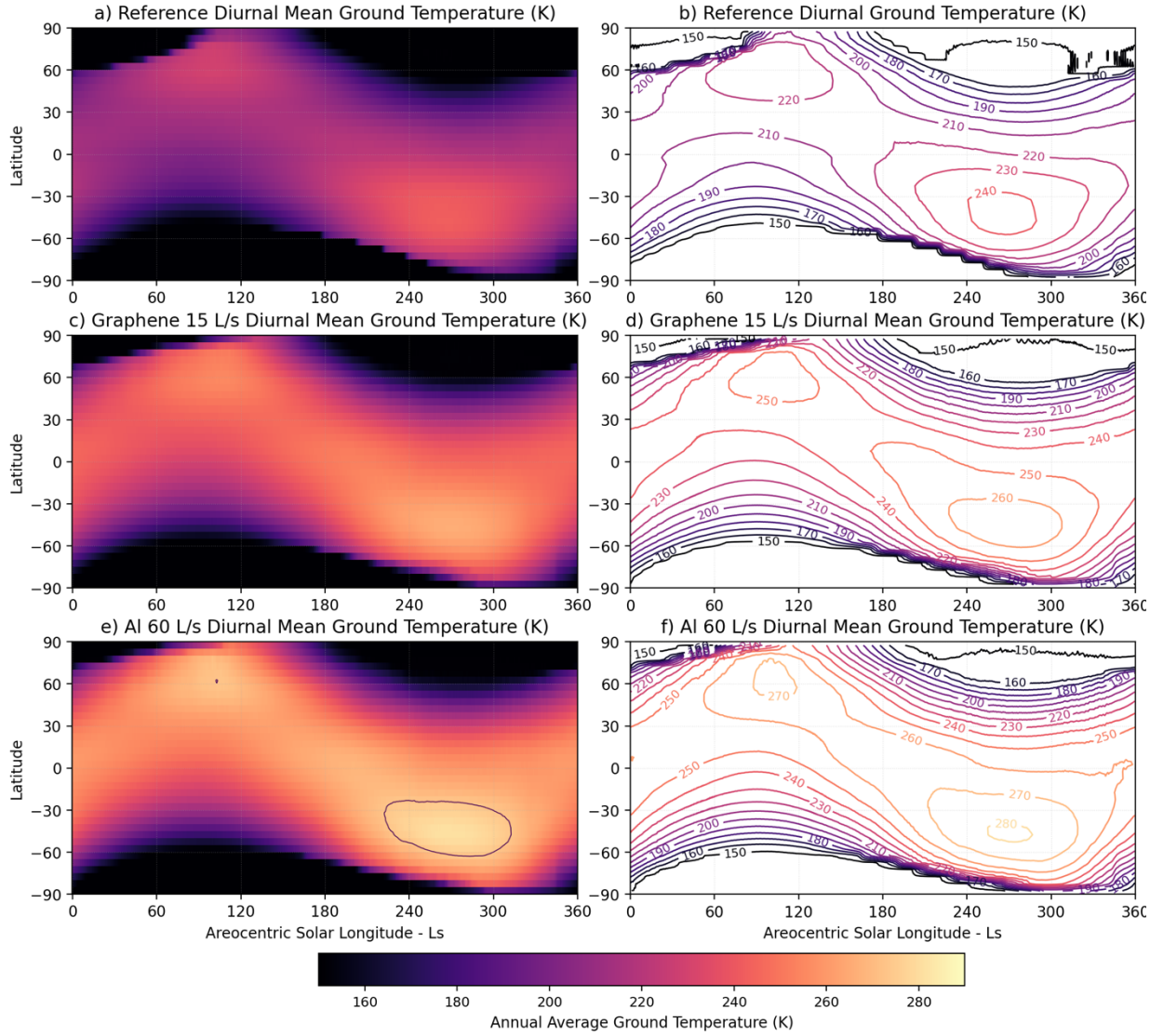

496 **Fig. S13. Seasonal variation of diurnally averaged surface temperature (K).** **(a,b)** Control
497 case (*run* Cc8). **(c,d)** Graphene case, 15 L/s (*run Cc41*). **(e,f)** Al particles, 60 L/s. (*run Cc16*). On
498 panel (c) the contour line encloses the latitude-time region of diurnally averaged temperature
499 about 273 K.

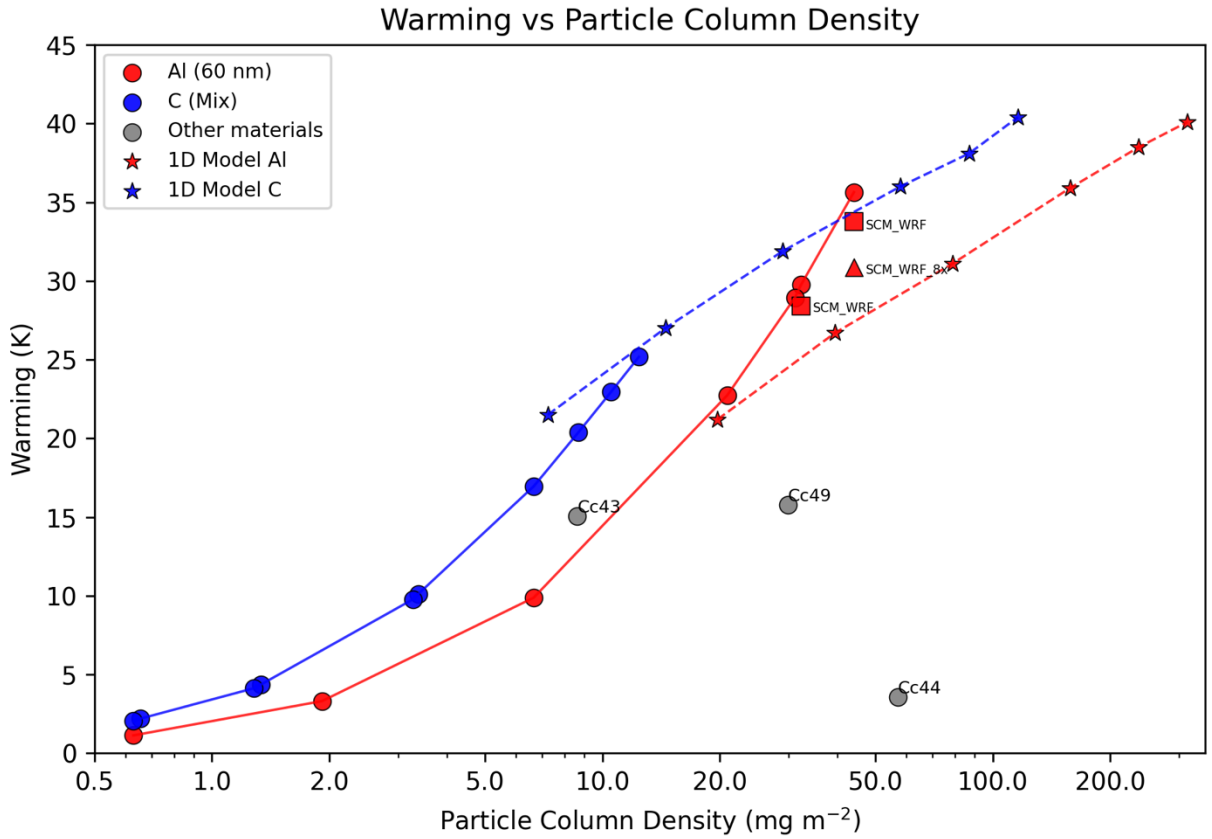

Fig. S14. Global warming as a function of particle column density. Comparison of 1D model output and WRF GCM 3D plume-tracking climate model output. Also shown are WRF Single Column Model (SCM) cases at GCM spectral resolution and at 8x spectral resolution (56 IR and 56 solar bands). Note that the 1D model no-warming temperature (the "zero" on this plot for the 1D runs) is 218 K, whereas the WRF 3D model no-warming temperature (the "zero" on this plot for the 3D runs) is 204.4 K. WRF SCM no-warming is 212.9 K (at both spectral resolutions).

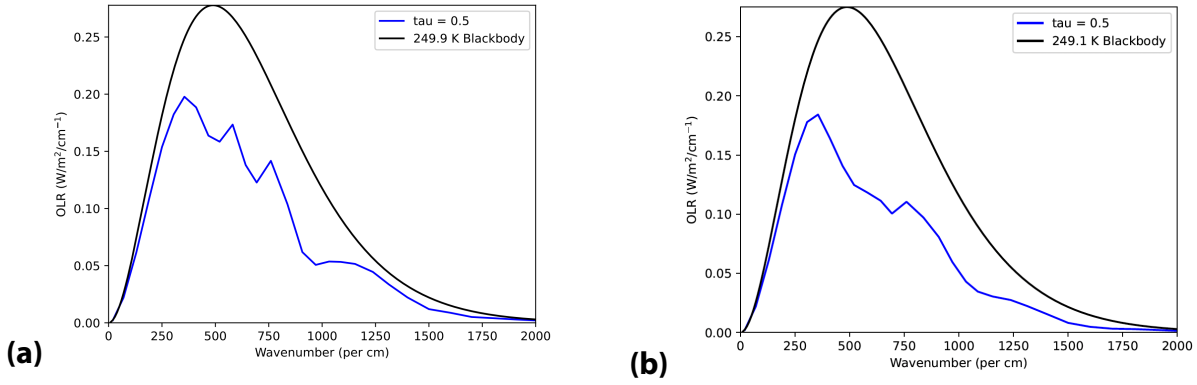

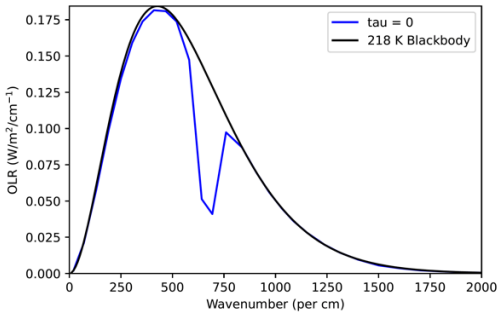

(c)

Fig. S15. Examples of spectrally resolved 1D climate model output. OLR = Outgoing Longwave Radiation. The blue curves correspond to the top-of-atmosphere thermal emission. The black curves correspond to the corresponding surface thermal emission. (a) Graphene (τ_{vis} = 0.5). (b) Al nanorods (τ_{vis} = 0.5). (c) No-warming case (this panel is reproduced from Ansari et al. 2024). 1D climate model output is summarized in Table S4.

508

509 **Supporting Tables.**

	Al rod (8 μm long × 60 nm × 60 nm)							
wavelength (μm)	scattering cross-section (m^2)	absorption cross-section (m^2)	asymmetry parameter, *g*		wavelength (μm)	scattering cross-section (m^2)	absorption cross-section (m^2)	asymmetry parameter, *g*
0.2	4.86E-13	4.46E-13	0.76182		27.784	4.52E-13	4.82E-13	0.017968
0.56778	3.30E-13	2.00E-13	0.62875		28.152	4.09E-13	4.80E-13	0.016856
0.93557	2.78E-13	1.24E-13	0.61122		28.52	3.72E-13	4.76E-13	0.016044
1.3034	3.11E-13	1.49E-13	0.60043		28.887	3.40E-13	4.70E-13	0.015525
1.6711	3.96E-13	2.02E-13	0.52437		29.255	3.12E-13	4.60E-13	0.015278
2.0389	3.79E-13	1.44E-13	0.59837		29.623	2.87E-13	4.47E-13	0.01527
2.4067	4.15E-13	1.68E-13	0.60509		29.991	2.64E-13	4.30E-13	0.015457
2.7745	5.92E-13	2.31E-13	0.50739		30.358	2.43E-13	4.11E-13	0.015788
3.1423	9.04E-13	4.58E-13	0.31906		30.726	2.25E-13	3.90E-13	0.016207
3.5101	1.11E-12	5.63E-13	0.36581		31.094	2.07E-13	3.68E-13	0.016665
3.8778	8.92E-13	5.21E-13	0.24		31.462	1.91E-13	3.45E-13	0.017119
4.2456	9.22E-13	4.79E-13	0.34226		31.829	1.77E-13	3.23E-13	0.017541
4.6134	1.67E-12	1.32E-12	0.27497		32.197	1.63E-13	3.01E-13	0.01792
4.9812	8.40E-13	4.08E-13	0.22821		32.565	1.51E-13	2.80E-13	0.018251
5.349	9.23E-13	4.01E-13	0.33662		32.933	1.39E-13	2.61E-13	0.018537
5.7168	1.37E-12	5.22E-13	0.30799		33.301	1.29E-13	2.44E-13	0.01878
6.0846	2.14E-12	1.62E-12	0.28861		33.668	1.19E-13	2.30E-13	0.018971
6.4524	1.62E-12	1.07E-12	0.16687		34.036	1.11E-13	2.17E-13	0.019094
6.8201	9.73E-13	5.21E-13	0.10957		34.404	1.03E-13	2.08E-13	0.019122
7.1879	9.21E-13	3.83E-13	0.18737		34.772	9.54E-14	2.00E-13	0.019019
7.5557	1.06E-12	5.03E-13	0.23115		35.14	8.90E-14	1.96E-13	0.018752
7.9235	1.19E-12	5.50E-13	0.21333		35.507	8.32E-14	1.93E-13	0.018297
8.2913	1.68E-12	7.03E-13	0.2203		35.875	7.80E-14	1.92E-13	0.017641
8.6591	2.40E-12	1.31E-12	0.23074		36.243	7.35E-14	1.94E-13	0.01679
9.0268	2.97E-12	2.17E-12	0.21556		36.611	6.94E-14	1.97E-13	0.015761
9.3946	3.01E-12	2.61E-12	0.17771		36.978	6.59E-14	2.01E-13	0.014583
9.7624	2.54E-12	2.17E-12	0.12243		37.346	6.28E-14	2.07E-13	0.01329
10.13	1.90E-12	1.33E-12	0.055812		37.714	6.01E-14	2.13E-13	0.011914
10.498	1.38E-12	7.55E-13	-0.007209		38.082	5.78E-14	2.21E-13	0.010486
10.866	1.11E-12	5.96E-13	-0.038166		38.45	5.58E-14	2.29E-13	0.0090313
11.234	1.04E-12	6.24E-13	-0.030053		38.817	5.41E-14	2.37E-13	0.0075691
11.601	1.07E-12	6.43E-13	-0.010819		39.185	5.26E-14	2.45E-13	0.0061152
11.969	1.13E-12	6.11E-13	0.0059081		39.553	5.14E-14	2.53E-13	0.0046804
12.337	1.18E-12	5.62E-13	0.019553		39.921	5.03E-14	2.60E-13	0.0032723
12.705	1.25E-12	5.44E-13	0.029777		40.289	4.94E-14	2.68E-13	0.0018958
13.072	1.36E-12	5.91E-13	0.037433		40.656	4.86E-14	2.74E-13	0.00055384
13.44	1.51E-12	7.15E-13	0.045057		41.024	4.79E-14	2.81E-13	-0.0007521
13.808	1.67E-12	8.97E-13	0.053475		41.392	4.73E-14	2.86E-13	-0.0020214
14.176	1.82E-12	1.09E-12	0.060761		41.76	4.68E-14	2.91E-13	-0.0032544
14.544	1.98E-12	1.24E-12	0.065881		42.127	4.63E-14	2.94E-13	-0.0044514
14.911	2.19E-12	1.34E-12	0.06997		42.495	4.58E-14	2.97E-13	-0.0056132
15.279	2.49E-12	1.40E-12	0.074165		42.863	4.54E-14	2.99E-13	-0.0067406
15.647	2.92E-12	1.50E-12	0.078465		43.231	4.50E-14	3.00E-13	-0.0078345
16.015	3.49E-12	1.71E-12	0.08234		43.599	4.45E-14	3.00E-13	-0.0088956
16.383	4.18E-12	2.09E-12	0.085375		43.966	4.41E-14	3.00E-13	-0.0099247
16.75	4.95E-12	2.68E-12	0.087416		44.334	4.36E-14	2.98E-13	-0.010922
17.118	5.71E-12	3.45E-12	0.088481		44.702	4.32E-14	2.95E-13	-0.011888
17.486	6.42E-12	4.34E-12	0.088671		45.07	4.27E-14	2.92E-13	-0.012824

17.854	7.00E-12	5.27E-12	0.088113		45.438	4.22E-14	2.88E-13	-0.013729
18.222	7.42E-12	6.14E-12	0.086934		45.805	4.16E-14	2.83E-13	-0.014603
18.589	7.66E-12	6.87E-12	0.085249		46.173	4.10E-14	2.77E-13	-0.015447
18.957	7.71E-12	7.39E-12	0.083162		46.541	4.04E-14	2.70E-13	-0.01626
19.325	7.58E-12	7.67E-12	0.080757		46.909	3.98E-14	2.63E-13	-0.017043
19.693	7.30E-12	7.70E-12	0.078108		47.276	3.91E-14	2.56E-13	-0.017795
20.06	6.90E-12	7.51E-12	0.075275		47.644	3.84E-14	2.47E-13	-0.018517
20.428	6.42E-12	7.11E-12	0.072306		48.012	3.77E-14	2.39E-13	-0.019208
20.796	5.87E-12	6.57E-12	0.069243		48.38	3.69E-14	2.29E-13	-0.019869
21.164	5.31E-12	5.92E-12	0.066116		48.748	3.62E-14	2.20E-13	-0.0205
21.531	4.74E-12	5.22E-12	0.062954		49.115	3.54E-14	2.10E-13	-0.021102
21.899	4.18E-12	4.51E-12	0.059778		49.483	3.45E-14	2.00E-13	-0.021675
22.267	3.66E-12	3.82E-12	0.056603		49.851	3.37E-14	1.90E-13	-0.022221
22.635	3.18E-12	3.19E-12	0.053444		50.219	3.28E-14	1.79E-13	-0.022739
23.003	2.75E-12	2.61E-12	0.050314		50.587	3.20E-14	1.68E-13	-0.023233
23.37	2.36E-12	2.12E-12	0.047221		50.954	3.11E-14	1.57E-13	-0.023701
23.738	2.02E-12	1.70E-12	0.044174		51.322	3.02E-14	1.46E-13	-0.024147
24.106	1.73E-12	1.36E-12	0.041183		51.69	2.93E-14	1.35E-13	-0.024571
24.474	1.48E-12	1.10E-12	0.038259		52.058	2.84E-14	1.24E-13	-0.024975
24.842	1.27E-12	8.94E-13	0.035412		52.425	2.75E-14	1.13E-13	-0.025359
25.209	1.09E-12	7.45E-13	0.032657		52.793	2.65E-14	1.03E-13	-0.025726
25.577	9.46E-13	6.40E-13	0.030013		53.161	2.56E-14	9.17E-14	-0.026075
25.945	8.23E-13	5.71E-13	0.027503		53.529	2.47E-14	8.10E-14	-0.026407
26.313	7.20E-13	5.27E-13	0.025154		53.897	2.38E-14	7.04E-14	-0.026724
26.68	6.34E-13	5.02E-13	0.022995		54.264	2.29E-14	5.99E-14	-0.027025
27.048	5.63E-13	4.89E-13	0.021058		54.632	2.20E-14	4.97E-14	-0.027311
27.416	5.03E-13	4.84E-13	0.019374		55	2.11E-14	3.96E-14	-0.027582

Table S1. Optical properties of engineered metal aerosol. Notes: Negative extinction cross sections are set to zero before use in the climate model. In code, albedos <0.01 and >0.99 are removed (i.e., albedo is bounded between those limits).

	Graphene (1000 nm-diameter graphene disk)		Graphene (250 nm-diameter graphene disk)			Graphene (1000 nm-diameter graphene disk)		Graphene (250 nm-diameter graphene disk)	
λ (μm)	scattering cross-section (m^2)	absorption cross-section (m^2)	scattering cross-section (m^2)	absorption cross-section (m^2)	λ (μm)	scattering cross-section (m^2)	absorption cross-section (m^2)	scattering cross-section (m^2)	absorption cross-section (m^2)
2.00E-07	4.51E-16	1.41E-14	2.47E-17	8.96E-16	7.14E-06	1.60E-17	9.59E-15	1.85E-20	5.16E-16
2.11E-07	5.47E-16	1.44E-14	3.04E-17	9.15E-16	7.22E-06	1.56E-17	9.35E-15	1.49E-20	5.19E-16
2.22E-07	7.93E-16	1.52E-14	4.47E-17	9.67E-16	7.30E-06	1.46E-17	9.14E-15	1.13E-20	5.22E-16
2.33E-07	1.48E-15	1.96E-14	8.41E-17	1.25E-15	7.38E-06	1.30E-17	8.98E-15	7.90E-21	5.26E-16
2.44E-07	2.86E-15	3.20E-14	1.64E-16	2.06E-15	7.46E-06	1.10E-17	8.88E-15	4.54E-21	5.29E-16
2.56E-07	4.41E-15	4.90E-14	2.53E-16	3.15E-15	7.53E-06	8.71E-18	8.84E-15	1.27E-21	5.33E-16
2.67E-07	5.08E-15	5.84E-14	2.90E-16	3.73E-15	7.61E-06	6.32E-18	8.85E-15	-1.91E-21	5.37E-16
2.78E-07	4.57E-15	5.57E-14	2.61E-16	3.53E-15	7.69E-06	3.96E-18	8.93E-15	-4.98E-21	5.41E-16
2.89E-07	3.44E-15	4.58E-14	1.97E-16	2.89E-15	7.77E-06	1.76E-18	9.05E-15	-7.95E-21	5.45E-16
3.00E-07	2.36E-15	3.59E-14	1.35E-16	2.26E-15	7.84E-06	-1.45E-19	9.21E-15	-1.08E-20	5.49E-16
3.78E-07	3.05E-16	1.40E-14	1.54E-17	8.71E-16	7.92E-06	-1.68E-18	9.39E-15	-1.36E-20	5.54E-16
4.56E-07	2.37E-16	1.26E-14	1.01E-17	7.93E-16	8.00E-06	-2.78E-18	9.59E-15	-1.62E-20	5.58E-16
5.33E-07	1.94E-16	1.14E-14	6.75E-18	7.13E-16	8.50E-06	1.33E-16	4.28E-15	2.04E-18	1.18E-15
6.11E-07	1.60E-16	1.07E-14	4.70E-18	6.57E-16	9.06E-06	1.77E-16	1.33E-14	4.37E-18	3.39E-15
6.89E-07	1.37E-16	1.02E-14	3.48E-18	6.35E-16	9.61E-06	1.86E-16	1.98E-14	6.91E-18	4.74E-15

7.67E-07	1.24E-16	1.00E-14	2.70E-18	6.23E-16	1.02E-05	1.40E-16	2.40E-14	2.09E-17	1.72E-14
8.44E-07	1.19E-16	9.83E-15	2.16E-18	6.15E-16	1.07E-05	1.23E-16	8.39E-15	2.77E-17	2.71E-14
9.22E-07	1.17E-16	9.72E-15	1.80E-18	6.12E-16	1.13E-05	1.95E-16	2.00E-14	1.67E-17	1.64E-14
1.00E-06	1.16E-16	9.81E-15	1.52E-18	6.05E-16	1.18E-05	1.60E-16	1.42E-14	5.77E-18	5.40E-15
1.08E-06	1.14E-16	9.71E-15	1.31E-18	6.12E-16	1.24E-05	1.99E-16	1.18E-14	2.39E-18	3.13E-15
1.16E-06	1.12E-16	9.77E-15	1.12E-18	5.94E-16	1.29E-05	2.86E-16	2.78E-14	1.84E-18	2.73E-15
1.23E-06	1.11E-16	9.69E-15	1.01E-18	6.06E-16	1.35E-05	2.73E-16	3.09E-14	1.16E-18	1.37E-15
1.31E-06	1.06E-16	9.64E-15	8.76E-19	6.07E-16	1.40E-05	2.55E-16	2.28E-14	5.64E-19	5.64E-16
1.39E-06	1.01E-16	9.42E-15	7.69E-19	5.78E-16	1.46E-05	3.49E-16	3.03E-14	4.07E-19	7.32E-16
1.47E-06	9.86E-17	9.59E-15	7.06E-19	5.93E-16	1.51E-05	4.89E-16	5.42E-14	4.30E-19	9.69E-16
1.54E-06	9.47E-17	9.68E-15	6.49E-19	6.18E-16	1.57E-05	5.58E-16	7.31E-14	3.72E-19	7.68E-16
1.62E-06	8.96E-17	9.58E-15	5.78E-19	6.01E-16	1.63E-05	5.60E-16	7.80E-14	2.32E-19	3.53E-16
1.70E-06	8.38E-17	9.35E-15	5.09E-19	5.66E-16	1.68E-05	6.10E-16	8.30E-14	1.16E-19	9.95E-17
1.78E-06	8.07E-17	9.40E-15	4.59E-19	5.62E-16	1.74E-05	8.17E-16	1.10E-13	8.08E-20	1.23E-16
1.86E-06	8.02E-17	9.98E-15	4.31E-19	5.90E-16	1.79E-05	1.19E-15	1.70E-13	1.03E-19	2.94E-16
1.93E-06	7.28E-17	9.67E-15	4.13E-19	6.22E-16	1.85E-05	1.65E-15	2.55E-13	1.33E-19	4.32E-16
2.01E-06	6.98E-17	9.38E-15	3.92E-19	6.30E-16	1.90E-05	2.07E-15	3.45E-13	1.36E-19	4.43E-16
2.09E-06	6.83E-17	1.01E-14	3.63E-19	6.12E-16	1.96E-05	2.34E-15	4.17E-13	1.09E-19	3.36E-16
2.17E-06	6.18E-17	9.22E-15	3.29E-19	5.81E-16	2.01E-05	2.42E-15	4.58E-13	6.63E-20	1.80E-16
2.24E-06	6.19E-17	1.01E-14	2.93E-19	5.55E-16	2.07E-05	2.31E-15	4.63E-13	2.74E-20	4.76E-17
2.32E-06	5.70E-17	9.28E-15	2.63E-19	5.46E-16	2.12E-05	2.05E-15	4.36E-13	4.14E-21	4.34E-17
2.40E-06	5.35E-17	9.93E-15	2.40E-19	5.56E-16	2.18E-05	1.72E-15	3.85E-13	-5.57E-22	4.34E-17
2.48E-06	5.51E-17	9.78E-15	2.25E-19	5.79E-16	2.23E-05	1.36E-15	3.23E-13	9.05E-21	3.61E-17
2.56E-06	4.63E-17	9.26E-15	2.16E-19	6.05E-16	2.29E-05	1.03E-15	2.59E-13	2.55E-20	1.12E-16
2.63E-06	4.85E-17	1.02E-14	2.12E-19	6.27E-16	2.34E-05	7.54E-16	2.00E-13	4.16E-20	1.83E-16
2.71E-06	4.80E-17	9.56E-15	2.10E-19	6.40E-16	2.40E-05	5.38E-16	1.50E-13	5.22E-20	2.30E-16
2.79E-06	3.97E-17	9.22E-15	2.08E-19	6.42E-16	2.46E-05	3.85E-16	1.12E-13	5.51E-20	2.44E-16
2.87E-06	4.07E-17	1.02E-14	2.04E-19	6.33E-16	2.51E-05	2.85E-16	8.45E-14	5.06E-20	2.29E-16
2.94E-06	4.37E-17	9.97E-15	1.98E-19	6.17E-16	2.57E-05	2.24E-16	6.65E-14	4.03E-20	1.90E-16
3.02E-06	3.76E-17	9.11E-15	1.90E-19	5.96E-16	2.62E-05	1.92E-16	5.56E-14	2.68E-20	1.38E-16
3.10E-06	3.20E-17	9.51E-15	1.79E-19	5.74E-16	2.68E-05	1.76E-16	4.98E-14	1.27E-20	8.20E-17
3.18E-06	3.46E-17	1.03E-14	1.66E-19	5.54E-16	2.73E-05	1.67E-16	4.71E-14	1.00E-22	3.15E-17
3.26E-06	3.77E-17	1.00E-14	1.52E-19	5.39E-16	2.79E-05	1.61E-16	4.60E-14	-9.61E-21	4.34E-17
3.33E-06	3.37E-17	9.21E-15	1.38E-19	5.30E-16	2.84E-05	1.52E-16	4.53E-14	-1.57E-20	4.34E-17
3.41E-06	2.71E-17	9.17E-15	1.24E-19	5.26E-16	2.90E-05	1.41E-16	4.44E-14	-1.81E-20	4.34E-17
3.49E-06	2.54E-17	9.92E-15	1.11E-19	5.28E-16	2.95E-05	1.26E-16	4.28E-14	-1.72E-20	4.34E-17
3.57E-06	2.91E-17	1.04E-14	9.92E-20	5.36E-16	3.01E-05	1.08E-16	4.05E-14	-1.36E-20	4.34E-17
3.64E-06	3.20E-17	1.01E-14	8.90E-20	5.47E-16	3.06E-05	8.86E-17	3.75E-14	-8.20E-21	4.34E-17
3.72E-06	2.97E-17	9.34E-15	8.04E-20	5.61E-16	3.12E-05	6.90E-17	3.40E-14	-1.77E-21	1.17E-17
3.80E-06	2.40E-17	9.02E-15	7.36E-20	5.77E-16	3.18E-05	5.02E-17	3.02E-14	4.91E-21	3.81E-17
3.88E-06	1.95E-17	9.39E-15	6.85E-20	5.94E-16	3.23E-05	3.33E-17	2.63E-14	1.12E-20	6.38E-17
3.96E-06	1.94E-17	1.01E-14	6.49E-20	6.10E-16	3.29E-05	1.89E-17	2.24E-14	1.67E-20	8.69E-17
4.03E-06	2.27E-17	1.05E-14	6.28E-20	6.25E-16	3.34E-05	7.42E-18	1.88E-14	2.10E-20	1.06E-16
4.11E-06	2.61E-17	1.03E-14	6.19E-20	6.39E-16	3.40E-05	-1.06E-18	1.56E-14	2.39E-20	1.20E-16
4.19E-06	2.66E-17	9.70E-15	6.21E-20	6.50E-16	3.45E-05	-6.59E-18	1.28E-14	2.55E-20	1.30E-16
4.27E-06	2.36E-17	9.16E-15	6.32E-20	6.59E-16	3.51E-05	-9.40E-18	1.05E-14	2.58E-20	1.34E-16
4.34E-06	1.87E-17	8.98E-15	6.49E-20	6.66E-16	3.56E-05	-9.84E-18	8.62E-15	2.48E-20	1.33E-16
4.42E-06	1.44E-17	9.25E-15	6.70E-20	6.70E-16	3.62E-05	-8.31E-18	7.25E-15	2.29E-20	1.28E-16
4.50E-06	1.28E-17	9.78E-15	6.95E-20	6.72E-16	3.67E-05	-5.25E-18	6.30E-15	2.01E-20	1.20E-16
4.58E-06	1.41E-17	1.03E-14	7.21E-20	6.71E-16	3.73E-05	-1.09E-18	5.74E-15	1.67E-20	1.08E-16
4.66E-06	1.73E-17	1.05E-14	7.47E-20	6.68E-16	3.78E-05	3.75E-18	5.51E-15	1.29E-20	9.51E-17
4.73E-06	2.05E-17	1.04E-14	7.72E-20	6.64E-16	3.84E-05	8.92E-18	5.54E-15	8.97E-21	8.05E-17
4.81E-06	2.23E-17	9.98E-15	7.96E-20	6.58E-16	3.89E-05	1.41E-17	5.77E-15	4.97E-21	6.53E-17
4.89E-06	2.17E-17	9.49E-15	8.17E-20	6.51E-16	3.95E-05	1.90E-17	6.16E-15	1.09E-21	5.00E-17

4.97E-06	1.91E-17	9.10E-15	8.35E-20	6.42E-16	4.01E-05	2.35E-17	6.65E-15	-2.54E-21	3.52E-17
5.04E-06	1.52E-17	8.94E-15	8.49E-20	6.33E-16	4.06E-05	2.74E-17	7.20E-15	-5.84E-21	2.12E-17
5.12E-06	1.13E-17	9.05E-15	8.60E-20	6.23E-16	4.12E-05	3.05E-17	7.76E-15	-8.74E-21	8.43E-18
5.20E-06	8.33E-18	9.36E-15	8.66E-20	6.13E-16	4.17E-05	3.29E-17	8.31E-15	-1.12E-20	4.34E-17
5.28E-06	7.08E-18	9.78E-15	8.68E-20	6.03E-16	4.23E-05	3.45E-17	8.82E-15	-1.32E-20	4.34E-17
5.36E-06	7.65E-18	1.02E-14	8.67E-20	5.93E-16	4.28E-05	3.54E-17	9.28E-15	-1.47E-20	4.34E-17
5.43E-06	9.68E-18	1.04E-14	8.61E-20	5.83E-16	4.34E-05	3.54E-17	9.66E-15	-1.57E-20	4.34E-17
5.51E-06	1.25E-17	1.05E-14	8.51E-20	5.74E-16	4.39E-05	3.48E-17	9.97E-15	-1.63E-20	4.34E-17
5.59E-06	1.54E-17	1.04E-14	8.38E-20	5.65E-16	4.45E-05	3.36E-17	1.02E-14	-1.64E-20	4.34E-17
5.67E-06	1.75E-17	1.02E-14	8.22E-20	5.56E-16	4.50E-05	3.18E-17	1.03E-14	-1.62E-20	4.34E-17
5.74E-06	1.86E-17	9.83E-15	8.02E-20	5.48E-16	4.56E-05	2.95E-17	1.04E-14	-1.57E-20	4.34E-17
5.82E-06	1.82E-17	9.47E-15	7.79E-20	5.41E-16	4.61E-05	2.68E-17	1.03E-14	-1.48E-20	4.34E-17
5.90E-06	1.66E-17	9.17E-15	7.54E-20	5.34E-16	4.67E-05	2.39E-17	1.02E-14	-1.37E-20	4.34E-17
5.98E-06	1.40E-17	8.97E-15	7.26E-20	5.28E-16	4.73E-05	2.06E-17	1.00E-14	-1.24E-20	4.34E-17
6.06E-06	1.09E-17	8.90E-15	6.96E-20	5.23E-16	4.78E-05	1.73E-17	9.76E-15	-1.09E-20	4.34E-17
6.13E-06	7.76E-18	8.97E-15	6.64E-20	5.19E-16	4.84E-05	1.38E-17	9.45E-15	-9.30E-21	4.34E-17
6.21E-06	4.98E-18	9.15E-15	6.31E-20	5.15E-16	4.89E-05	1.03E-17	9.10E-15	-7.61E-21	4.34E-17
6.29E-06	2.92E-18	9.41E-15	5.96E-20	5.12E-16	4.95E-05	6.82E-18	8.70E-15	-5.88E-21	4.34E-17
6.37E-06	1.80E-18	9.72E-15	5.61E-20	5.10E-16	5.00E-05	3.42E-18	8.27E-15	-4.12E-21	4.34E-17
6.44E-06	1.69E-18	1.00E-14	5.24E-20	5.08E-16	5.06E-05	1.34E-19	7.82E-15	-2.37E-21	4.34E-17
6.52E-06	2.52E-18	1.03E-14	4.86E-20	5.07E-16	5.11E-05	-3.00E-18	7.34E-15	-6.62E-22	2.26E-18
6.60E-06	4.12E-18	1.04E-14	4.49E-20	5.06E-16	5.17E-05	-5.95E-18	6.86E-15	9.96E-22	8.07E-18
6.68E-06	6.26E-18	1.05E-14	4.11E-20	5.06E-16	5.22E-05	-8.70E-18	6.37E-15	2.58E-21	1.38E-17
6.76E-06	8.65E-18	1.05E-14	3.72E-20	5.07E-16	5.28E-05	-1.12E-17	5.88E-15	4.08E-21	1.94E-17
6.83E-06	1.10E-17	1.05E-14	3.34E-20	5.08E-16	5.33E-05	-1.35E-17	5.39E-15	5.48E-21	2.48E-17
6.91E-06	1.31E-17	1.03E-14	2.96E-20	5.09E-16	5.39E-05	-1.56E-17	4.91E-15	6.77E-21	2.99E-17
6.99E-06	1.47E-17	1.01E-14	2.59E-20	5.11E-16	5.44E-05	-1.74E-17	4.44E-15	7.94E-21	3.48E-17
7.07E-06	1.57E-17	9.84E-15	2.21E-20	5.14E-16	5.50E-05	-1.89E-17	3.99E-15	9.00E-21	3.93E-17

Table S2. Optical properties of modeled graphene disks. Asymmetry parameter is close to zero. (Negative cross-sections are set to zero before use in the climate model).

Material	run_name	Release Site	Release Rate (L/s)	Warming (K)	Average Ground Temperature (K)	Particle Column Density (kg/m2)	Average Surface Pressure (Pa)	Warm Season Temperature in 47.5S Band (K)	Steady State Annual Mean Particle Visible Optical Depth
	reference - Cc8			0	204.4	0	625.67	241.8	0
Al (60 nm)	Cc32	Equatorial	1	1.13	205.50	6.29E-07	626.85	242.87	4.01E-03
Al (60 nm)	Cc31	Equatorial	3	3.31	207.68	1.91E-06	629.28	244.96	1.22E-02
Al (60 nm)	Cc30	Equatorial	10	9.88	214.25	6.67E-06	639.64	251.61	4.25E-02
Al (60 nm)	Cc29	Equatorial	30	22.74	227.11	2.09E-05	667.30	265.63	1.33E-01
Al (60 nm)	Cc17	Equatorial	45	29.76	234.13	3.23E-05	680.13	273.49	2.06E-01
Al (60 nm)	Cc16	Equatorial	60	35.64	240.00	4.41E-05	689.01	280.29	2.81E-01
C (Mix)	Cc36	Equatorial	1	2.20	206.57	6.56E-07	625.26	243.86	9.47E-03
C (Mix)	Cc35	Equatorial	2	4.37	208.73	1.33E-06	627.11	245.95	1.93E-02
C (Mix)	Cc34	Equatorial	5	10.12	214.48	3.38E-06	636.93	251.55	4.88E-02
C (Mix)	Cc33	Equatorial	12.5	20.38	224.75	8.68E-06	662.42	262.44	1.25E-01
C (Mix)	Cc41	Equatorial	15	22.96	227.32	1.05E-05	666.81	265.34	1.52E-01
C (Mix)	Cc42	Equatorial	17.5	25.18	229.54	1.24E-05	671.94	267.88	1.79E-01
Al (60 nm)	Cc15	Mid-Lat	45	28.94	233.31	3.11E-05	679.89	272.41	1.99E-01
C (Mix)	Cc9	Mid-Lat	1	2.04	206.40	6.28E-07	623.58	243.67	9.07E-03
C (Mix)	Cc12	Mid-Lat	2	4.13	208.50	1.28E-06	624.74	245.58	1.85E-02
C (Mix)	Cc10	Mid-Lat	5	9.78	214.15	3.28E-06	635.70	251.02	4.73E-02
C (Mix)	Cc13	Mid-Lat	10	16.96	221.32	6.67E-06	656.54	258.62	9.64E-02
C (1000 nm)	Cc43	Equatorial	15	15.05	219.42	8.63E-06	642.58	255.82	7.48E-02
C (250 nm)	Cc44	Equatorial	100	3.58	207.94	5.71E-05	632.85	246.00	3.05E-02
Al (160 nm)	Cc49	Equatorial	45	15.76	220.13	2.99E-05	656.30	258.52	1.43E-01

Table S3. Summary of 3D plume-tracking climate model output for runs to steady state, including sensitivity tests. For Release Site: "Mid-Lat" is Arcadia, 40°N, 202°E. "Equatorial" is Elysium, 0°N, 135°E. “C (mix)” refers to a mix of 16:1 (by number) 250 nm-diameter graphene disks to 1000 nm-graphene disks. For the last three rows, “Al (160 nm)” refers to the 9 µm × 160 nm × 160 nm particles modeled in Ansari et al. (2024), and “C (1000 nm)” and “C (250 nm)” refer to the sensitivity tests shown in Fig. S5. Warm-season temperature is defined as the average temperature during the warmest 70-sol period of the year.

526

Optical depth @ 0.67 μm, τ_{vis}	Column mass (mg/m^2) (Graphene)	T_{surf} (K)	Albedo	OLR (W/m^2)
0	0	218.0	0.2178	114.10
0.125	7.25	239.5	0.1301	127.39
0.25	14.5	245.0	0.0804	134.58
0.5	29	249.9	0.0335	142.54
1	58	254.0	0.0087	145.52
1.5	86.9	256.1	0.0048	145.52
2	115.9	258.4	0.0041	147.86
Optical depth @ 0.67 μm, τ_{vis}	Column mass (mg/m^2) (Al rods)	T_{surf} (K)	PALB	OLR (W/m^2)
0	0	218.0	0.2178	114.1
0.125	19.6	239.2	0.1993	117.62
0.25	39.3	244.7	0.1861	119.96
0.5	78.5	249.1	0.1693	121.66
1	157.1	253.9	0.1531	124.76
1.5	235.7	256.5	0.1468	125.37
2	314.2	258.1	0.1444	125.152

527

528 **Table S4.** Summary of 1-D model output. PALB = planetary albedo.
529 OLR = Outgoing Longwave Radiation.